Sedimentary Geology 427 (2022) 106038

Contents lists available at ScienceDirect

Sedimentary Geology

journal homepage: www.elsevier.com/locate/sedgeo

Depositional and diagenetic model of the Aptian potash-bearing Loémé evaporites in onshore Congo

Laurent Gindre-Chanu [a,*], Alexandre Pichat [b], Vincent Delhaye-Prat [c], Chantal Vis [d], Roland Ringenbach [d], Jean-Marie Schlund [d]

[a] TERRA GEOSCIENCES, 3 Bis rue des Marmuzots, 21000 Dijon, France
[b] E2S-UPPA, Total, CNRS, Univ. Pau & Pays Adour, Laboratoire des Fluides Complexes et leurs Réservoirs-IPRA, UMR5150, 64013 Pau, France
[c] TOTALENERGIES, CSTJF, avenue Larribau, 64000 Pau, France
[d] KALIVIE MUSEUM, Avenue Joseph-Else, 68310 Wittelsheim, France

ARTICLE INFO

Article history:
Received 2 August 2021
Received in revised form 29 October 2021
Accepted 29 October 2021
Available online 9 November 2021

Editor: Dr. Catherine Chagué

Keywords:
Republic of Congo
Facies
Diagenesis
Evaporites
Potash
Bromine trace elements

ABSTRACT

The evaporites of the Aptian Loémé Formation occur along the stable structural domain of onshore Congo as horizontally well-stratified depositional halite interbedded with Mg-poor potash minerals including carnallite, bischofite, tachyhydrite and sylvite. Eleven correlative depositional recharge-to-evaporation cycles are composed of suites of organic-prone shale followed by primary halite and carnallite beds, sometimes punctuated by a bischofite-tachyhydrite end-member.

A sedimentological and petrographical analysis performed on cores and thin sections allowed an interpretation of nine facies associations, named as FA1 to FA9, relying upon the occurrence of bands of fluid inclusions, grain-size, dissolution features, detrital sediments, minute inclusions and sedimentary structures. A depositional model reconciles the spatial distribution of primary textures, hydrology, brine saturation and palaeo-depth during a standard regressive evaporation cycle. Shallow burial eo-diagenesis led to compaction-driven dissolution and recrystallization into fine-grained halite and carnallite laminites but poorly affected the overall preservation of primary deposits.

Measurements and profile analysis of bromine trace element concentrations reveal a palaeo-salinity increase of the parent brine for cycle II to base IX caused by a relative brine level fall and a gradual confinement of the salt basin, likely associated with an excess of saline elements inflow from hydrothermal vents. Similar depositional textures and bromine concentration variations are observed in the lower cycles of the Aptian evaporites from the counter-part Sergipe Basin in the northern part of the Brazilian margin, testifying of a progressive brine salinity rise due to a palaeogeographic confinement along the northern segment of the South Atlantic Ocean.

In Congo, the sylvite displays horizontal "pseudo-stratifications" that unconformably overlay the crests of anticlines and propagate along flanks as a sharp-based caprock. The flushing and transformation of depositional carnallite – halite into secondary sylvite – halite is interpreted as having been caused by down-stepping incremental dissolutions sourced by younger pervasive connate to phreatic waters. In Sergipe, the sylvite is interpreted as secondary but further results from syndepositional dissolution of carnallite and tachyhydrite due to a regional North Atlantic Ocean ingression.

1. Introduction

Understanding the origin and distribution of evaporites along the South Atlantic margins of Africa and South America is important for defining the salt palaeogeography during the Aptian rift-to-drift evolution. Several studies propose large-scale palinspastic and climatic scenarios to describe the connectivity of Aptian salt basins (Dias, 2005; Rouchy and Blanc-Valleron, 2006; Davison, 2007; Torsvik et al., 2009; Moulin et al., 2010; Chaboureau et al., 2012) but the relationships between primary evaporite textures, parent brine hydrology and depositional palaeo-bathymetry have not been thoroughly described. Moreover, although the role of hydrothermal activity in the occurrence of Ca-rich potash is of growing scientific interest (Hovland et al., 2006; Cheng et al., 2019; Debure et al., 2019; Fernandez et al., 2020), the issue of the palaeo-salinity evolution with respect to relative brine level variations, brine composition and basin confinement in time is unresolved.

* Corresponding author.
E-mail address: laurent_gindre@yahoo.fr (L. Gindre-Chanu).

https://doi.org/10.1016/j.sedgeo.2021.106038
0037-0738/

Recent work performed on the Ibura member of the Sergipe Basin in the North-East Brazil (Szatmari et al., 2021) has shed some light on the mode of formation of the Aptian evaporites along the northern segment of the South Atlantic, by showing geochemical relationships between primary fabrics and a parent brine possibly enriched with calcium by hydrothermal inflow. There, the sylvite is diagenetic, resulting from the early leaching of depositional carnallite and tachyhydrite, caused by a northern ingression of Central Atlantic Ocean seawater during the Lower Albian (110.64 ± 0.34 M.y.), therefore indicating a palaeogeographic change at the end of evaporite deposition.

The potash-bearing evaporites of the Loémé Formation that extensively occur along the stable structural domain of onshore Congo and South Gabon are interpreted as a counterpart to the Brazilian Ibura Member. The Loémé Fm consists of horizontally bedded primary halite with interbedded carnallite and bischofite-tachyhydrite that has conserved their original depositional fabrics without being affected by halokinesis or meso- to telogenetic dissolution (Belmonte et al., 1965; De Ruiter, 1979; Teisserenc and Villemin, 1990; Hirlemann, 1993; Hirlemann and Jaillard, 1993).

The lithostratigraphy of the Loémé Fm has been established during several decades of muriate mining operations (SRK Consulting, 2011, 2012; Pedley et al., 2016; Van Der Klauw et al., 2019). Few geochemical studies that quantify the Aptian brine composition and palaeotemperature are available (Timofeeff et al., 2006; Zhang et al., 2017), and no studies have been made on the depositional textures of halite and carnallite that reconcile lateral facies changes, brine salinity and palaeo-depth. Most of the research in the region has focused on the mined sylvinite (mixture of the minerals sylvite and halite) because of its K_2O content, which is among the highest in the World. As in Brazil (Szatmari et al., 2009, 2021), the sylvite is considered to be the secondary by-product of carnallite, but its mechanism and timing of formation are poorly constrained. This lack of knowledge induced pitfalls in the interpretation of original composition and salinity of the Aptian brine in the northern part of the Atlantic margin.

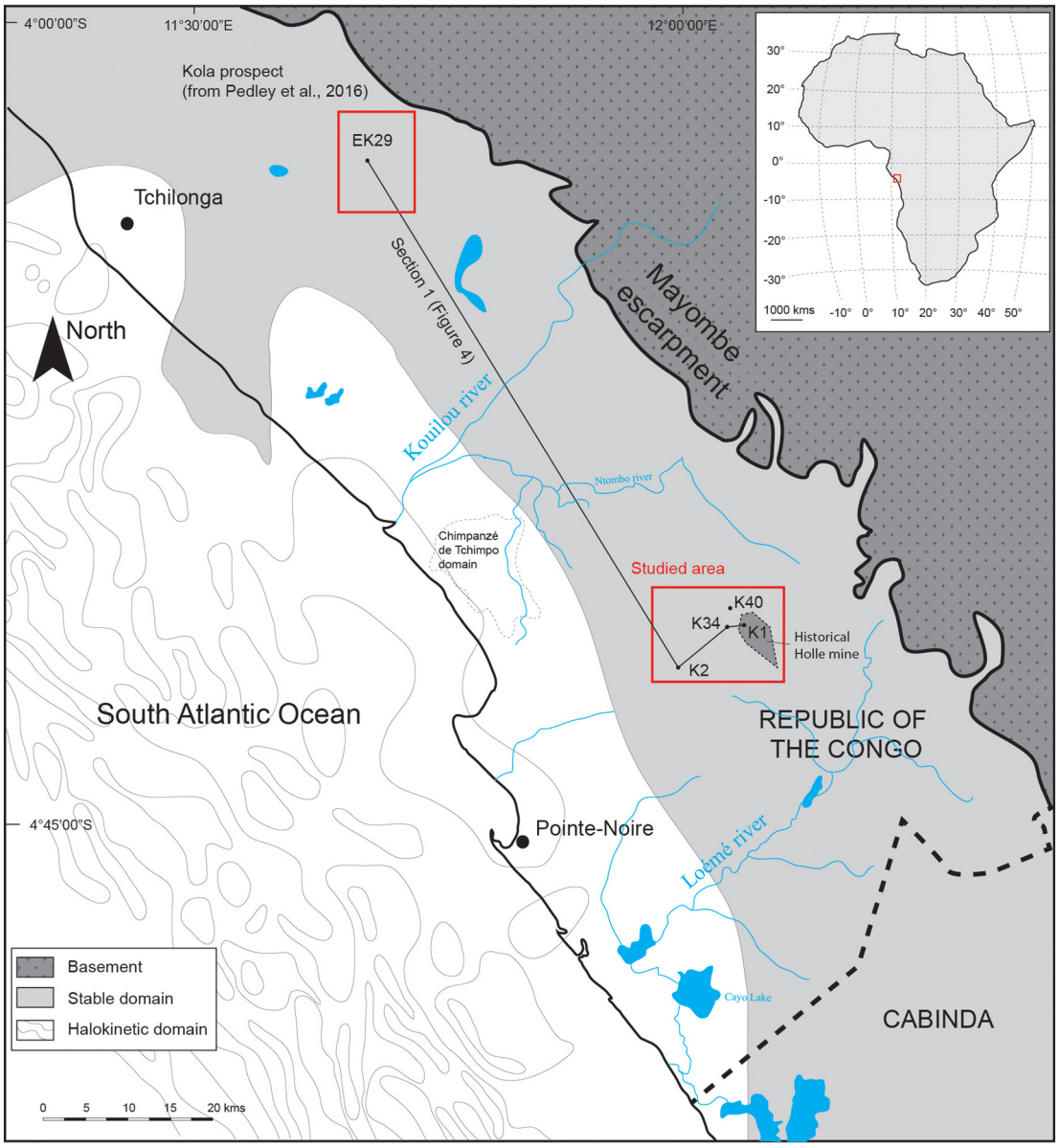

Fig. 1. Location map of the studied area in the South Kouilou region of onshore Republic of Congo. The historical Holle mine and Kola prospect are located along the stable domain defined by Reyre (1984). K1, K2, K34, K40, and EK29 are borehole locations.

The Mines de Potasses d'Alsace (MDPA) acquired a substantial amount of subsurface data in the Kouilou region of Congo between the 1960's and the closure of the Holle mine in 1977. The mine was closed after complete flooding by fresh water seeping downward. The MDPA rock repository archives preserved the halite, carnallite and sylvite of the Loémé Fm, although bischofite-tachyhydrite is too soluble to have been preserved. We use sedimentological, petrographical and geochemical analyses to (1) establish a depositional model that synthesizes primary fabrics, brine hydrology and palaeo-bathymetry of depositional halite and carnallite of the Aptian Loémé evaporites, (2) evaluate the palaeo-salinity evolution of the parent brine and (3) refine the model of formation of secondary sylvite. The question of whether the mother brine composition and salinity among the different Aptian salt sub-basins along the South Atlantic Margin are similar is crucial for establishing the Aptian post-break-up palaeogeography. We compare primary and diagenetic facies of the Loémé Fm with its counter-part evaporites in Brazil, known in the Sergipe Basin, to provide some key elements to re-examine the connectivity of hypersaline brines in the northern part of the South Atlantic Margin.

2. Geographical and geological background

The present-day distribution and lateral continuity of the Aptian evaporites along the western African margin represents a single giant salt basin extending from north Gabon to south Angola (Dias, 2005; Rouchy and Blanc-Valleron, 2006; Davison, 2007). The northern boundary of the basin is located near the Ascension Fracture Zone, north of the Gabon Basin (Davison, 2007), while the southern boundary is assumed to be the north of the Walvis Ridge, where Aptian mounded platform carbonates have been identified (Coterill et al., 2002). Along strike, the stable domain of onshore Congo and the southern part of Gabon shows few effects of halokinesis for more than 200 km (Reyre, 1984). The Loémé Fm displays a regional layered-cake configuration with horizontally stratified potash-bearing evaporites (Belmonte et al., 1965; De Ruiter, 1979; Teisserenc and Villemin, 1990). Westward, the complete original lithostratigraphy and depositional facies of the evaporites are destroyed due to significant roll-over, salt gliding and diapirism. In onshore Congo, the Kouilou region palaeogeographically corresponds to the easternmost coastal margin of the West African salt basin (Davison, 2007) (Fig. 1). In the subsurface, evaporites abut the faulted-bounded Proterozoic Mayombe basement by onlap (Pedley et al., 2016).

The study area is located onshore between the northern Kouilou and southern Loémé rivers in the Prefecture of Kouilou, in the southern part of the Republic of the Congo. The Holle mine is situated approximatively 40 km north-eastward of Pointe-Noire and about 10 km from surface exposures of Mayombe basement (Fig. 1).

3. Evaporite stratigraphy

The evaporites of the Aptian Loémé Fm that occur onshore Congo are among the most heterogeneous Cretaceous saline successions in the world (Warren, 2006). They are only known from subsurface data and mainly consist of halite (NaCl) with interbedded Mg-poor potash deposits including carnallite ($KMgCl_3$, $6H_2O$), bischofite ($MgCl_2$), tachyhydrite ($CaCl_2$, $2MgCl_2$, $12H_2O$) and sylvite (KCl) (Fig. 2) (Lambert, 1967; De Ruiter, 1979; Teisserenc and Villemin, 1990; SRK Consulting, 2011, 2012; Pedley et al., 2016; Van Der Klauw et al., 2019;). Anhydrite is strikingly rare, only occurring as metre-thick cap rocks and in thin seams scattered within the succession (Belmonte et al., 1965; De Ruiter, 1979). Carnallite and bischofite-tachyhydrite deposits, are interpreted as primary, while sylvite is considered as secondary mineral formed from the dissociation of carnallite by penetrative less saline fluids (Wardlaw and Nicholls, 1972; Pedley et al., 2016). The overall thickness of the Loémé Fm along the onshore Congo margin varies between less than 50 m and about 950 m, depending on the eastward thinning related to the coastal onlap and *per descensum* dissolutions by post-salt phreatic waters (Belmonte et al., 1965; Pedley et al., 2016).

When they are poorly affected by dissolution, the Loémé evaporites are composed of 11 correlative depositional cycles, named I through XI, interpreted as solar-driven evaporation cycles, from 15 m to 130 m thick (Belmonte et al., 1965; Lambert, 1967; Brink, 1974; De Ruiter, 1979) (Figs. 2, 3). Each cycle is typified by a mineralogical succession consisting of basal dolomitic and bituminous shale, followed by halite, then a series of carnallite and halite beds (Belmonte et al., 1965; De Ruiter, 1979). A mixture of bischofite/tachyhydrite end-members terminate the tops of Cycles V, VI, VII and X (Hirlemann and Jaillard, 1993) (Fig. 2). Basal bituminous shales have been reported as being regional stratigraphical surfaces for correlations (Lambert, 1967). Potash seams are named using the historic nomenclature of MDPA, referring to the cycles within which they occur (*e.g.* cycle II, IV, IX, *etc.*) (Hirlemann and Jaillard, 1993; Pedley et al., 2016). Sylvite is commonly preserved at the top of anticlines, just below the anhydrite caprock (Fig. 3).

Post-salt sediments consist of Albian anhydrite and dolomitic limestones, followed by Cenomanian to Turonian interbedded dolomitized sands and shales (Fig. 2). Massive Maastrichtian conglomerates and Cenozoic sands account for the youngest sediments of the study area. At Holle, the shallowest post-salt aquifer consists of phreatic groundwater that flows towards Pointe-Noire through Maastrichtian and Cenozoic sands (Moukolo, 1992; Moukandi Nkaya et al., 2014), whereas the deepest one is made up of stagnant weakly saline phreatic water trapped in the Albian anhydritic carbonates (B.R.G.M., 1982). Some connate waters were also identified in the deeper aquifer (Pedley et al., 2016; SRK Consulting, 2012).

4. Age of the evaporites

The evaporites of the Loémé Fm are commonly dated between Upper Aptian to Lower Albian (Poropat and Colin, 2012). These ages are based on ostracod and pollen assemblages discovered in the uppermost pre-salt strata of Gabon and Cabinda (Grosdidier et al., 1996; Braccini et al., 1997; Bate, 1999; Bate et al., 2001) and planktonic foraminifera (*i.e. Hedbergella sp*; *Leopoldina cabri*) found just above the salt in the offshore Benguela Basin (Caron, 1978; Davison, 2007).

Field investigations of the Pre-Salt Vembo shales of the Chela Fm cropping out along the escarpments beside the Mayombe basement in the coastal plain of Congo have reported a significant density of pollens, ostracods, insects and dinoflagellates, typical of the AS12 biozone of Grosdidier et al. (1996). This confirms a Lower Aptian age for the sedimentary precursors prior to evaporites deposition (Delhaye-Prat et al., 2016). In onshore Gabon, the discovery of *Deshayesites consobrinoïdes* (Hourcq and Devigne, 1950) at the base of the Madiela Fm (equivalent of the Congolese post-salt series argilo-dolomitiques) indicates the overburden is from the Upper Aptian. Based on all biological elements inventoried from Angola to Gabon from the literature, the Loémé Fm seems best attributed to the Middle to Upper Aptian.

5. Data and methods

We constructed a complete sedimentological section from cycle II to the top of cycle IX from slabbed cores of the K1 borehole, with additional observations made from core samples of the K39, K54 and K55 boreholes. Halite, carnallite and sylvite fractions were examined petrographically relying on an analysis of 50 thin sections, and details of the carnallite textures were observed using a scanning electron microscope equipped with a Brucker Quantax EDS detector (SEM-Quantax, TOTAL CSTJF Laboratory). Chemical compositions were analysed by high accuracy μ-EDSat with a resolution of 2–3 μm/pixel. The evaporites from the lowermost cycle I, the uppermost cycle X, and the anhydrite caprock could not be examined because of the lack of cores.

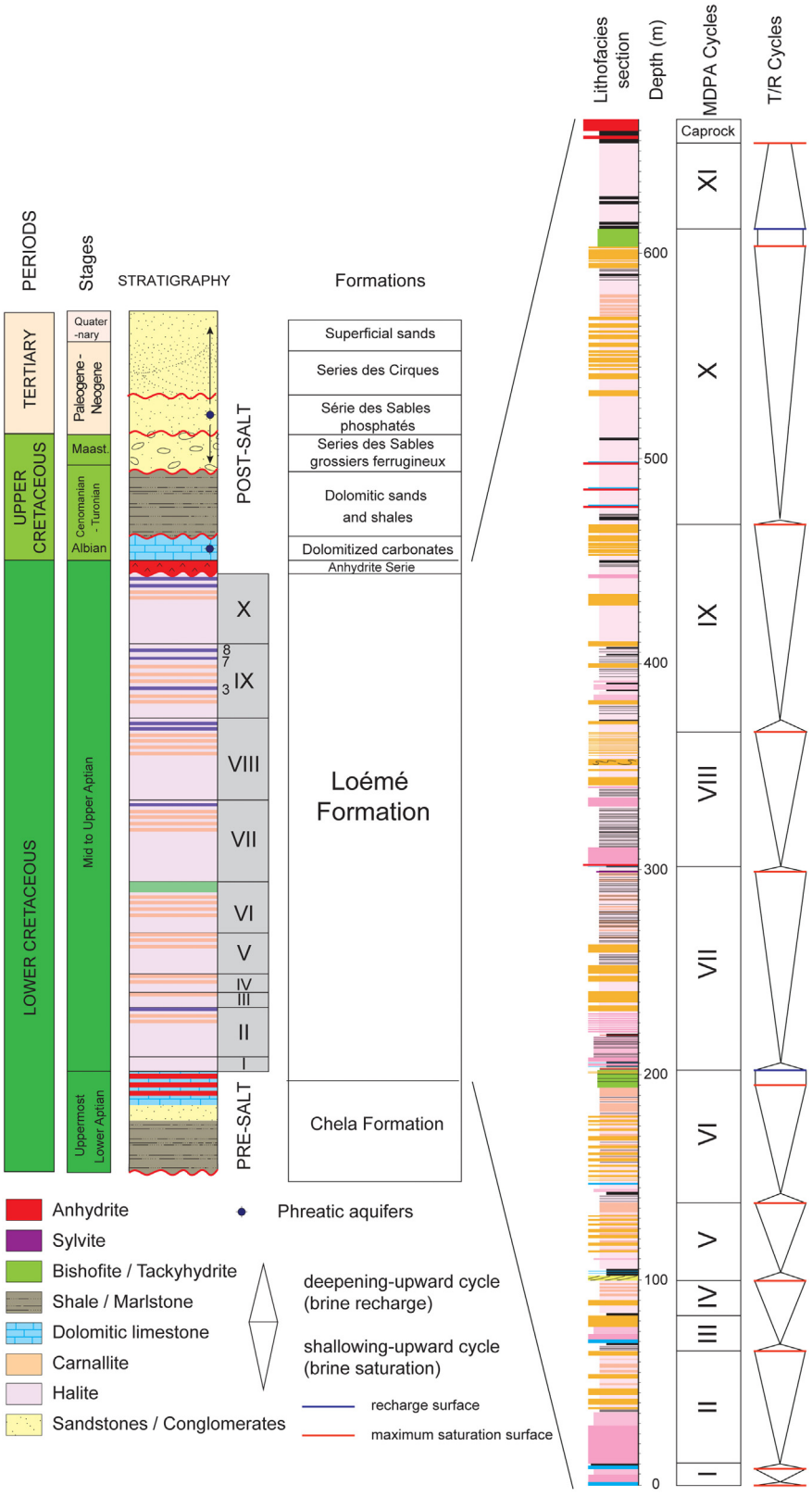

Fig. 2. Regional stratigraphy of the onshore South Congo and detailed lithofacies section of the Aptian Loémé evaporites. The regional correlative depositional cycles of MDPA are labelled I to XI. The synthetic section of the subsurface potash-bearing Loémé evaporites is a composite of K1, K44 and PN2 boreholes to discard secondary sylvite occurrence at the top of the Formation.

Total bromine was measured for 561 samples from bulk rocks of the borehole K40 between the base of the cycle II and the top of the cycle IX. Samples were cleaned with distilled water at ambient temperature in laboratory. The bromine analysis was carried out by X-ray fluorescence. All measurements are expressed in ppm with a standard deviation of <5%. Bulk rock measurements account for the total bromine concentration of salt samples, including bromine content incorporated by each chloride fraction that composes the salt rock, fluid inclusions and

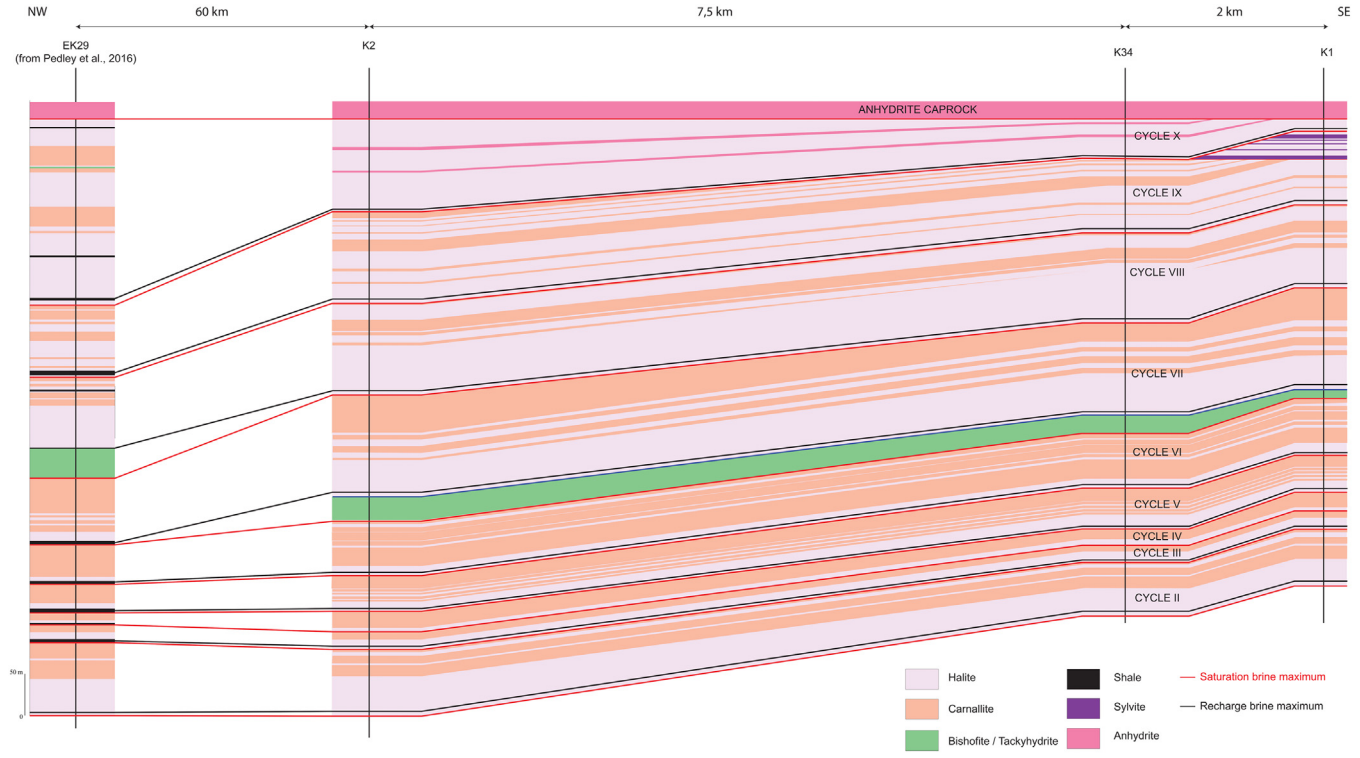

Fig. 3. Northwest-southeast (NW-SE) borehole correlation section (see Fig. 1 for location).

recrystallised textures. In order to determine the bromine content of the prevalent chloride mineral, respective proportions of halite and carnallite were calculated for each sample. Total bromine trace element concentrations respectively measured for halite and carnallite fractions were corrected from lithological proportions relative to each sampled bed. According to Wardlaw and Schwerdtner (1966), Moretto (1988) and Cathro et al. (1992), we have estimated that the bromine content entrapped into fluid inclusions and paragenetic textures can reach in zoned halite between 19% to 41% of bulk samples measurements, depending on fluid inclusions density and the rate of remobilised bromine elements into recrystallised cements.

6. Facies associations

Nine facies associations within the shale, halite, carnallite and sylvite have been distinguished. The main characteristics and interpretations of facies associations (FAs) are highlighted as followings:

6.1. FA1: black organic-rich shale

Centimetre to decimetre thick, very black shales with varying organic matter content occur at the base of each MDPA depositional cycle (Fig. 3), either above a disconformable surface capping the potash of the previous cycle or above thinly halite overlaying the basal surface (Fig. 4A). Shales are thinly-laminated and transition upwards into fine or coarse-grained halite. A fish fossil, approximately 8 cm long, belonging to the *Pleuropholidae* group has been found at the base cycle III in the K26 well (Fig. 4B).

The shales are interpreted as having settled during major brine recharges enabling the subsequent saturation sequences. Recharges are interpreted as less saline water flooding, leading to a progressive return of adequate trophic conditions for the invasion of halophile organisms (Evans and Kirkland, 1988). The recharges led to relative rises of water column that probably became density-stratified. Anoxic conditions prevailed at shallow brine bottom favouring preservation of the organic matter preservation (Warren, 1986).

6.2. FA2: very coarse-grained clear bottom-growth halite - zoned cumulates

White to brown centimetre across halite cubes form cm-thick blankets of bottom-growth crystals conformably followed by medium to very coarse-grained, cm-thick halite cumulate layers (Fig. 4C, D). Basal halite grows freely as euhedral crystals devoid of fluid inclusions. Cumulates, made up of millimetre across hoppers and rafts, enclose large alternating bands of whitish, milky halite that ranges from rich to poor in fluid inclusions (Fig. 4D, E). Cuboids and cumulates facies associations form centimetre to decimetre thick repetitive couplets that stack to form metre-thick bands of pure halite without interbedded dolomicritic or shaly laminae and without dissolution surfaces. Cumulates stack to form a granoblastic texture with mostly sutured grain to grain contacts (Fig. 4F). FA2 is commonly observed above the shales at the base of MDPA cycles.

Abundant stripes of fluid inclusions in fine-grained cumulates were formed by the daily warming and cooling alternation of brine (Benison and Goldstein, 1999), whereas the coarser inclusions-free chevrons and cuboids indicate growth in a thermally stable brine body, less influenced by temperature fluctuations (Cathro et al., 1992; Benison and Goldstein, 2000; Hovorka et al., 2007). The elongate bottom-growth halite of FA2 gradually passes upwards into zoned cumulate beds without an erosional surface or dolomicrite/mud draping, suggesting that crystal nucleation operated from the brine floor in subaqueous conditions sheltered from dissolution, freshening, and detrital influxes (Schreiber, 1988; Hovorka et al., 2007). The couplets marked by bottom-growth halite and draping milky cumulates record a progressive salinity rise of a brine that probably evolved from low to high halite saturation (Schreiber and El Tabakh, 2000). According to Sirota et al. (2017, 2018), the low-to high halite saturation might may be related to seasonal variations of brine temperature.

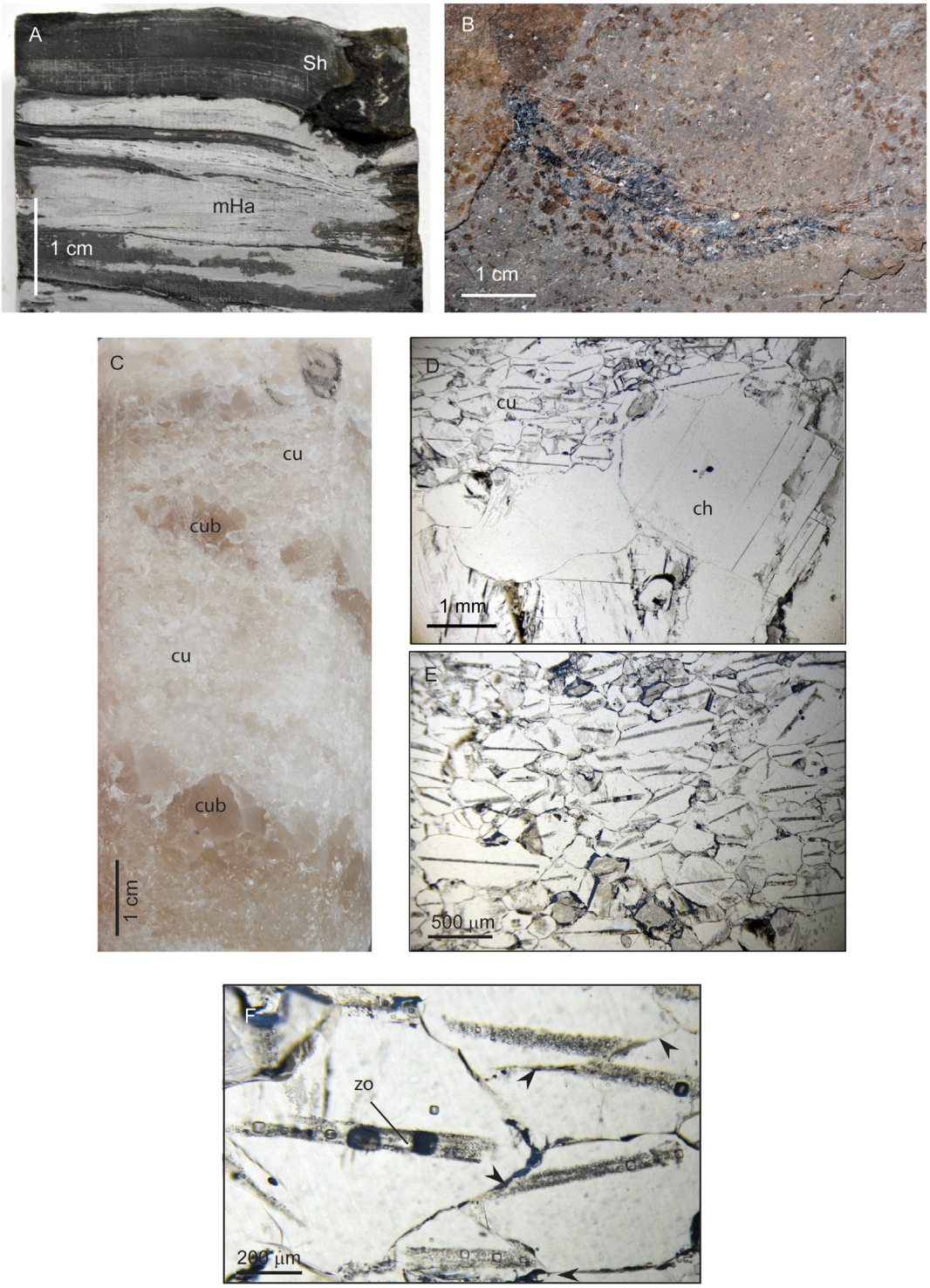

Fig. 4. Photographs of macro- and micro-facies of shale, anhydrite and halite fabrics (FA1 and FA2). A) Organic matter rich shale (Sh, FA1) overlaying very fine-grained halite (mHa, K1 well, 690.80 m, base cycle II). B) Fossilized fish (*Pleuropholidae group*) preserved in black shale (FA1) (K16 well, base cycle III). C) Clear very coarse bottom-growth cuboid halite (cub) and coarse zoned cumulates (cu) (FA2) (K1 well, 668.20 m, cycle III). D) Clear chevrons (ch) conformably overlain by zoned cumulates - rafts (cu) (K1 well, 667.35 m, cycle III). E) Granoblastic texture made up of zoned rafts accumulation (K1 well, 667.35 m, cycle III). F) Details of zoned (zo) rafts-to-rafts suture (black arrow).

6.3. FA3: medium-grained zoned bottom-growth halite - dolomicrite - halite laminites

FA3 comprises three different types of facies: (i) basal millimetric to centimetric bottom-growth and cloudy halite crystals, (ii) very thin dolomicrite/shale laminae and (iii) fine to medium-grained halite cumulates (Fig. 5A, B, C, D, E).

FA3 is subdivided in two groups: FA3a and FA3b which respectively differ in the lack or the occurrence of discrete planar to undulose dissolution surfaces that may occur at the contact between the top of coarse to fine-grained halite and the base of dolomicrite (Fig. 5C, E). In FA3a, coarse skeletal halite and cumulates are equally preserved (Fig. 5A). Bottom-growth halite crystals grow freely on dolomicrite, forming coarsely crystalline layers with a rough serrated top.

Basal coarse to very coarse cloudy halite crystals are made up of elongated vertically grown banded chevrons and cornets that form crystalline bouquets with either pointing or widening crests and narrow intergrowth space respectively (Fig. 5A). Cuboid clusters show masses of chaotically organised crystals, locally displacing surrounding layers (Fig. 5A). In thin section, both FA3 fabrics display euhedral zoned crystals that enclose alternating stripes parallel to crystal faces that are rich or poor in fluid inclusions (Fig. 5B). Edges of bottom-growth halite and adjacent inter-crystalline spaces are commonly cemented by clear displacive halite (Fig. 5B).

Grey to yellowish thinly laminated dolomicrite and shale, either gradually drapes the pointing crests of coarse halite crystals in FA3a (Fig. 5A) or unconformably relies on a planar dissolution surface in FA3b (Fig. 5C, E).

Millimetre up to 1 cm across zoned halite cumulates gradually overlay dolomicrite layers, forming a granoblastic well-sorted texture.

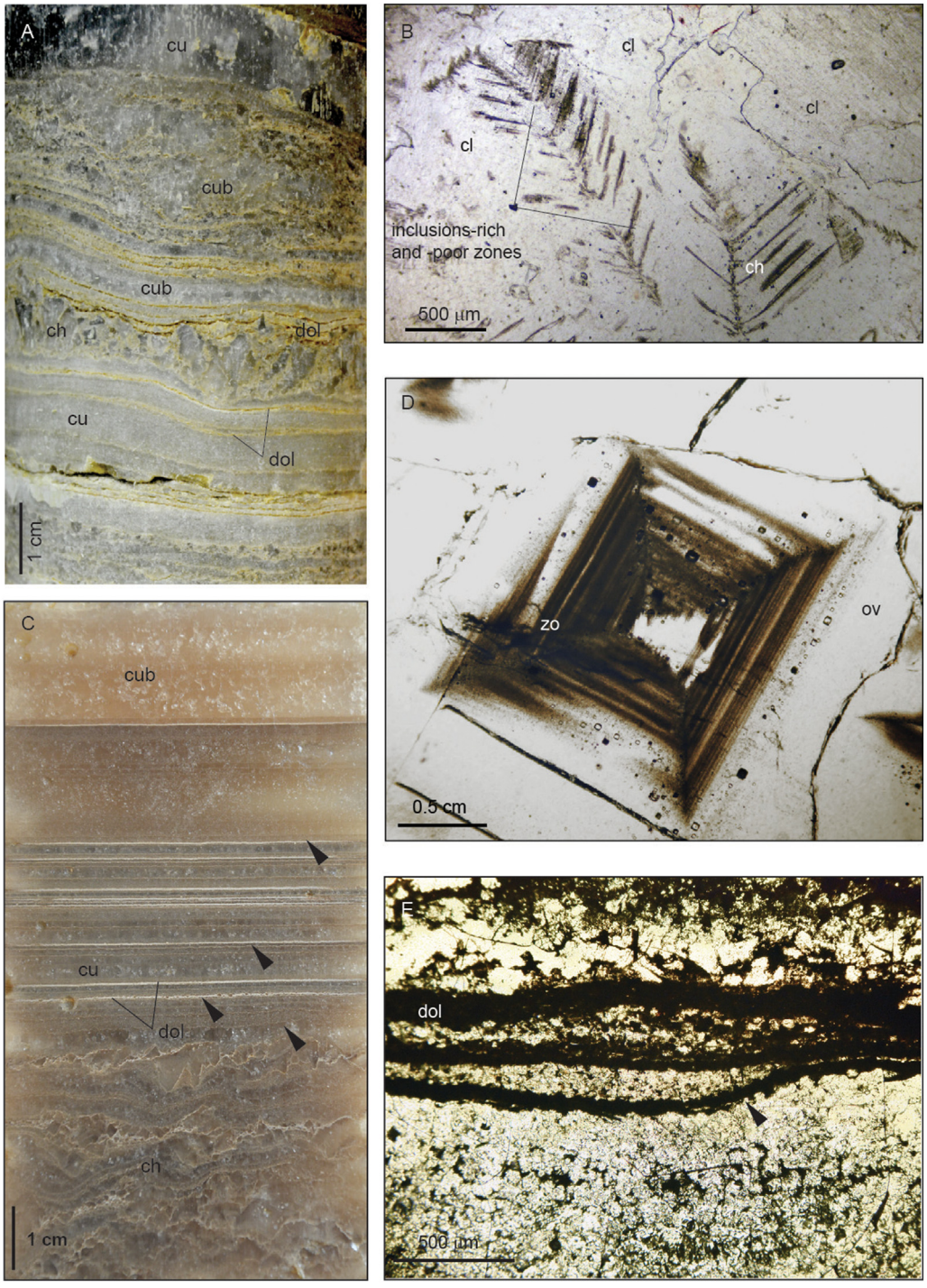

Fig. 5. Photographs of facies and micro-facies of FA3. A) Coarse-grained bottom-nucleated zoned halite chevrons (ch) and cuboids (cub), dolomicritic laminae sets (dol) and microcrystalline zoned cumulates (cu) (FA3a) (K1 well, 654 m, cycle IV). B) Zoned chevrons (ch) truncated by a dissolution surface overlain by clear halite cement (cl) (FA3a) (K54 well, 336.58 m, base cycle IX). C) Coarse-grained zoned cuboids (cub), chevron (ch) and fine grained halite cumulates (cu) bounded by planar dissolution surfaces (black arrows) and dolomicrite laminae (dol) (FA3b) (K1 well, 632 m, cycle IV). D) Close-up of a zoned halite hopper (zo) and overgrowth (ov). E) Close-up of a dissolution surface (black arrow) truncating halite cumulate and draped by dolomicrite (dol) (FA3b) (K1 well, 629 m, cycle IV).

Crystals are euhedral, with well-preserved inclusions banding and fringed by clear syntaxial overgrowth (Fig. 5D). Zoned hoppers commonly show re-entrants and voids subsequently filled by clear halite.

FA3a differs from FA2 because it contains zoned bottom-growth crystals conformably draped by dolomicrite and shale laminae, indicating that the original brine underwent (1) temperature variations during halite crystallisation at pond floor and (2) was episodically diluted by under-saturated inflows responsible for thin detrital deposition.

Brine ponding facilitated the *syn*-crystallisation of clustering halite cubes within a still porous laminated halite host, as testified by the occurrence of displacive nodular structures in deformed laminites. In FA3b, the planation surfaces, reduction of bottom-growth halite thickness at the expense of laminites, and the larger abundance of solution voids and re-entrants all indicate a brine environment further marked by freshening episodes and dissolution as compared to FA3a (Shearman, 1970; Lowenstein and Hardie, 1985; Casas and Lowenstein, 1989; Schubel and Lowenstein, 1997; Sirota et al., 2020).

6.4. FA4: fine-grained zoned bottom-growth halite – dolomicrite – halite laminites

The FA4 mainly consists of well-sorted horizontal to undulating laminites made up of (i) basal mm-thick dolomicrite, (ii) anhydrite seams gradually overlain by (iii) centimetric laminae of very fine to fine-grained halite crystals (Fig. 6A, B). Millimetric displacive nodules randomly crystallised into the laminated halite host. Fine halite and dolomicrite lamina sets form "varves". FA4 fabrics are subdivided into two distinct fabrics, respectively showing conformable and parallel couplets (FA4a) or symmetrical wave-ripple structures with local disconformities (Fig. 6B). Both fabrics systematically alternate with thick carnallitic beds in the upper part of the MDPA cycles.

In thin section, dolomicrite encloses abundant subhedral to euhedral isolated halite cubes, hoppers or platy flakes, with average crystal sizes ranging from 20 to 50 mm (Figs. 6C, 7A), whereas the anhydrite laminae show tiny anhydrite laths and needles. Centimetre-thick halite laminites are composed of euhedral to subhedral, cloudy or clear crystals, with grain sizes ranging from 10 to 400 μm across, displaying a microcrystalline well-sorted granoblastic texture.

Cloudy halite grains occur in both FA4a and FA4b fabrics and consist of closely-packed skeletal hoppers and platy flakes that individually display alternated bands that are rich- and poor- in fluid inclusions (Fig. 7B, C). Overgrowth commonly occurs as syntaxial halite spar that is poor in fluid inclusions. Zoned halite and overgrowths show smoothed U-shaped re-entrants and voids filled by sparry clear halite without residue, mud or anhydrite coating (Fig. 7C). The contacts between halite crystals vary from curved to sharp bevel-like sutures, accounting for local dissolution surfaces.

FA4a may display clear euhedral to anhedral halite grains devoid of bands of fluid inclusions and overgrowth. They form sutures with abundant minute mineral inclusions including (i) floating pelletoidal to stellate polyhalite (Fig. 7D), (ii) altered anhydrite laths, (iii) quartz grains (Fig. 7E) or (iv) polyhedral dull dolomite crystals with cubic nuclei (Fig. 7F). Inclusions are either poïkilotopically cemented by halite or positioned at grain boundaries, filling the inter-crystalline space.

Dolomicrite and anhydrite laminae accumulated during short-lived freshening episodes, whereas banded halite hoppers, plates and rafts formed at a quiet brine-air interface or within the upper brine column when the degree of brine saturation increased. Fine-grained zoned halite laminites commonly result from periodic influxes of fresher water followed by hypersaline concentration of a standing brine body where daily temperature variations are recorded (Warren, 2006), whereas clear halite cumulates would rather precipitate in a deeper brine body where daily temperature variations show less contrasts (Rosell Ortiz and Ortí Cabo, 1981-1982). Before sinking to the floor by gravity, cumulates grow, may merge to form rafts and episodically undergo minor surficial freshening, leading to local dissolution of still floating zoned textures. FA4a indicates halite accumulation upon a hypolimnetic or mixed brine floor, unaffected by waves, storm reworking or dissolution by freshening events.

FA4b deposits were further controlled by an epilimnetic or stratified brine, as testified by the flat dissolution surfaces at the base of couplets. Moreover, wave-rippled structures indicate that halite crystals were deposited above the fair-weather wave base (see Dellwig and Evans, 1969; Weiler et al., 1974; Gornitz and Schreiber, 1981).

FA4b is similar to wavy laminites deposited in the Dead Sea during 2012–2013, when poorly consolidated fine-grained halite and detrital mud were mobilised by wave action in shallow epilimnetic stratified brine (Sirota et al., 2017, 2020). However, the abundance of enclosed polyhedral dolomite, quartz and anhydrite needles in both FA4a and FA4b fabrics reveal detrital input related to fresh waters inflows into a shallow water environment and to land proximity.

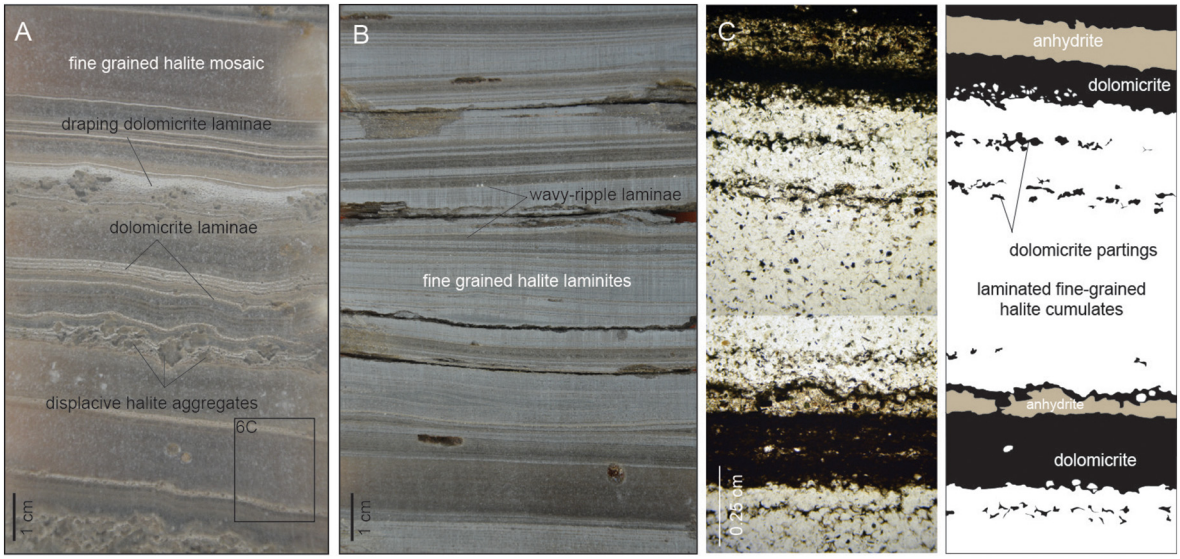

Fig. 6. Photographs of facies association FA4. A) Thinly-laminated clear microcrystalline halite alternating with dolomicritic and anhydritic laminae (FA4a). Note the displacive halite cubes that locally deform layers (K1 well, 629.50 m, cycle V). B) Wave-rippled microcrystalline halite laminites (FA4b). C) Details of dolomicrite – anhydrite –clear microcrystalline halite suite illustrated in the panel A (F4b).

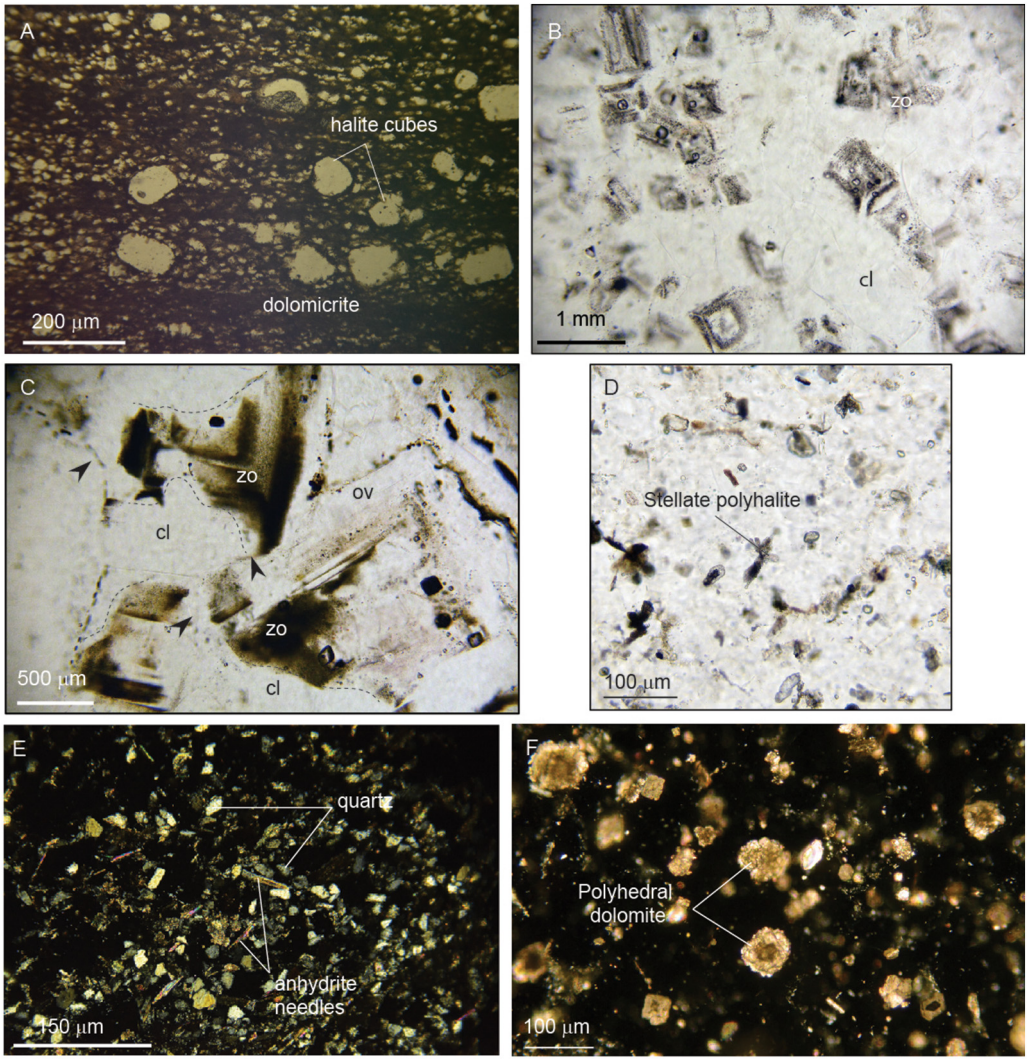

Fig. 7. Photographs of FA4 micro-facies. A) Dolomicrite laminae with enclosed clear halite cube. B) Granoblastic mosaic of zoned hoppers (ho) with clear halite (cl). (K34 well, 301.42 m, cycle). C) Aggregates of zoned hoppers (zo) with overgrowth (ov) truncated by clear halite (cl). Black arrows underline dissolution surfaces (K39 well, 297.03 m, cycle IX). D) Stellate polyhalite enclosed into fine-grained halite cumulates. E) Poorly-sorted aggregates of anhydrite needles and quartz grains cemented by halite. F) Polyhedral dolomite crystals floating into microcrystalline halite.

Burial-related compactional features readily occurred in fine to coarse-grained laminites, where pressure-solution and subsequent recrystallisation probably led to the formation of strained grain-to-grain sutures and clear displacive halite in inter-crystalline pore spaces (Fig. 7A, B). Similar sharp solutional contacts and clear halite cement were interpreted as early diagenetic features operating into a formerly porous halite host during shallow burial, prior to reaching a depth of 40 m (Casas and Lowenstein, 1989). In addition, density-driven reflux may have also induced clear halite crystallisation in pore spaces but would have remained effective in shallow burial until salt beds got completely occulted by compaction (Spencer et al., 1990).

6.5. FA5: red bottom-growth carnallite – halite laminites

This facies consists of very red to orange bottom-nucleated untwinned crystals of carnallite that freely grew on fine-grained halite laminites as centimetre-long, upright bi-pyramidal crystals (Fig. 8A). Crystal boundaries are well defined, linear to regular without abrasion features. Additionally, small fine to very coarse-grained displacive carnallite nodules are commonly seen enclosed in the laminated halite host. Individual crystals may group to form larger porphyroblasts, displacing the halite matrix outwards.

In thin section, bottom-growth carnallite crystals form large tinted individual porphyroblasts, whereas nodular carnallite textures consist of sparry cements that may enclose laminated dolomicritic or even halite crystals. Crystals are tinted in red by randomly dispersed hematite inclusions either within crystals or along cleavage planes.

Similar elongate pyramidal carnallite crystals perpendicular to and draped by halite laminites have been described in the Aptian Ibura member along the conjugate Brazilian margin by Wardlaw (1972) and Szatmari et al. (2009), and also along halite shorelines of artificial ponds of the southern Dead Sea (see https://www.saltworkconsultants.com/quaternary-potash/).

These textures have been interpreted as primary depositional carnallite fabrics resulting from highly concentrated parent brine that reached the carnallite saturation threshold. Crystals are intact, unaltered by dissolution or physical reworking and are free of detrital mud draping, suggesting crystallisation at the pond floor under hypolimnic conditions, sheltered from wave to wind and terrestrial inflows. Appositively, halite cumulates formed at or nearby surface during subsequent brine freshening, before sinking by gravity conformably on bottom-growth carnallite.

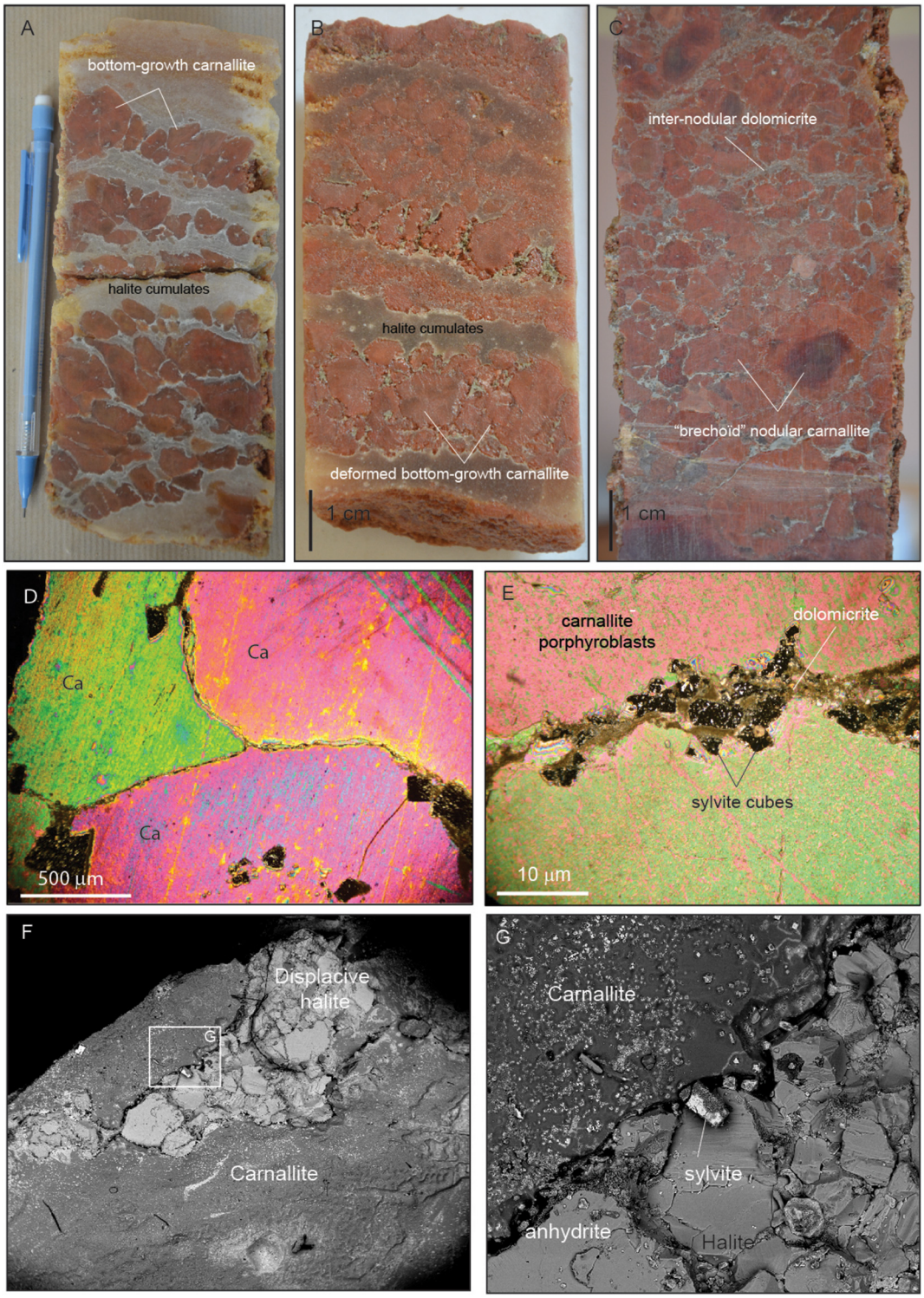

Fig. 8. Photographs of FA5 and FA6 facies and micro-facies. A) Depositional bottom-growth carnallite (K1 well, 686 m, cycle II). B) Deformed primary bottom-growth carnallite (K1 well, 675.67 m, cycle II). C) Nodular "brecchoid" carnallite (K1 well, 660 m, cycle II). D) Sutured nodular carnallite (ca) (polarized light) (K50 well, 654.29 m, cycle II). E) Weathered sparry carnallite rimmed at crystal boundary by sylvite cubes and dolomicrite (K54 well, 336.41 m, cycle IX). F) & G) SEM photographs displaying displacive halite infilling re-entrant in carnallite nodule and fringing sylvite cube (K50 well, 654.29 m, cycle II).

6.6. FA6: red nodular mosaic carnallite ("brecchoid") – halite laminites

FA6 consists of layered red to orange millimetre to centimetre diameter nodular carnallite enclosed and draped by thin microcrystalline halite. Carnallite crystals show a large spectrum of fabrics, ranging from spherical to ovoid, imparting a "brecchoid" fabric that conspicuously mimic primary bottom-growth carnallite crystals of FA5 (Fig. 8A, B, C). In thin section, carnallite forms large, rounded to ovoid, cm to 500 µm across tinted spars that are highly birefringent and present a sharp extinction under polarized light (Fig. 8D).

Like bottom-growth crystals, the nodular carnallite is coloured by red hematite inclusions, often lined up along cleavage planes (Fig. 8E).

Grain-to-grain contact varies from sutural to curvy, with concavo-convex shapes, straight, or even crenulated with localised deep re-entrants (Fig. 8E, F). Crenulated rims are locally underlined by tiny clear replacive sylvite cubes, while the pronounced re-entrants are filled by displacive halite (Fig. 8F, G). Less tinted anhedral carnallite crystals up to 30 μm across, or dolomicrite mesh, locally occur in the inter-crystalline space, where the carnallite contacts are not completely sutured (Fig. 8D).

FA6 form centimetre to decimetre thick parallel and layered thinning-upwards sequence sets that commonly occur at the base of the carnallitic units in the MDPA cycles (Fig. 3).

The "brecchoid" aspect of bedded nodular carnallite is documented in the literature but rarely interpreted (Szatmari et al., 1979, 2009, 2021; El Tabakh et al., 1999; Qiu et al., 2017). Although a minority of small displacive carnallitic nodules hosted in halite laminites indicates inter-crystalline growth by brine ponding, the coarser crystals resemble bottom-growth textures (Fig. 8A, B, C). Compared to FA5, the large crystals of FA6 are highly altered and display dissolution features (numerous solutional re-entrants and voids) that impart to the euhedral crystals a more rounded aspect. Accordingly, the edges of bottom-nucleated carnallite crystals have been smoothed by dissolution caused by less-saturated brine inflows. The brine dissolution also induced the deposition of anhydrite mesh and displacive clear halite linings, as with primary halite fabrics (see Shearman, 1970 and references therein). The dissolution led to the surficial decomposition of carnallite and subsequent *in situ* recrystallisation into sylvite cubes. We do not see evidence of carnallite recrystallisation as reported by Szatmari et al. (2021), but we do see fringing dissolution and deformation of crystals that led to the merger of crystals to form bedded nodular layers. Recrystallisation would have led to the loss or a change of hematite arrays alignment (Urai and Boland, 1985). Carnallite becomes geochemically unstable with burial-related temperature and pressure increases (Koeler et al., 1990; Koeler, 1997) and becomes mechanically weaker than halite (Urai et al., 2008), causing slight deformation prior to breakdown and incongruent dissolution into sylvite. Accordingly, the nodules of carnallite probably formed from primary bottom-growth crystals as a combined effect of *syn*-depositional alteration by freshening events followed by shallow burial-deformation without secondary recrystallisation.

6.7. FA7: red to white very fine-grained carnallite mosaic

FA7 consists of centimetre- to millimetre-thick horizontal laminites composed of very fine-grained well-sorted euhedral to subhedral red carnallite and microcrystalline zoned halite (Fig. 9A). The carnallite crystals have an average grain sizes of ca 100 μm, displaying polygonal to hexagonal shapes with grain-to-grain contacts ranging from straight to concavo-convex (Fig. 9B, C). Under natural light, the grains are tinted by abundant reddish to brownish iron oxides inclusions, varying from rounded to polygonal grains and very thin needles 100 μm or smaller in size (Fig. 9D). They nucleate from crystal centres as small structureless masses that progressively radiate towards the edges of the crystals with diverging alignments (Fig. 9E). 1 to 10 μm size clear carnallite crystals, devoid of hematite, commonly occur between the coarser tinted crystals as incipient grains, either isolated or arranged in clusters.

White translucid to pale red medium-grained carnallite layers are locally interbedded with the red carnallitic laminites (Fig. 9F). These layers display a patchwork of medium- to coarse-grained glomerular carnallite porphyroblasts, between 10 and 200 μm across (Fig. 9G). The crystals are commonly horizontal elongated and display irregular concavo-convex curved boundary. Nuclei form red-coloured patches, whereas crystal rims are lightly tinted.

FA7 forms centimetre- to decimetre-thick, horizontally-layered, fining-upwards sets that commonly occur at the top of carnallitic units of the MDPA cycles (Fig. 2).

The euhedral morphology of crystals, the small grain-size homogeneity and sorting, the distribution of prevalent red iron oxides (hematite) along crystalline growth planes suggest a depositional origin of carnallite cumulates (Rosell and Pueyo, 1997; Szatmari et al., 2009; Pueyo et al., 2017).

Carnallite precipitated in a highly saturated brine body as a dense "rain" of fine-grained crystals before accumulating at the floor by gravity. Although this carnallite does not show dissolution surfaces, detrital mud deposits or wave ripples, the carnallite may have been periodically subjected to dilution caused by rainfall, leading to the *in situ* dissolution of red cumulates, the redistribution of iron oxides, and the subsequent recrystallisation into more translucid to white porphyroblasts (Fig. 9F, G). Any freshening with concomitant detrital deposits would have been recorded by an erosional disconformity between both red to translucid layers and draping by preservation of thin mud.

As with FA4, the grain-to-grain sutures and adjacent clear carnallite sub-grains between red euhedral crystals indicate compaction-derived pressure-solution, with subsequent recrystallisation into inter-crystalline pores during shallow burial.

6.8. FA8: white translucid to red coarse-grained carnallite and zoned halite

FA8 occurs in the upper part of the cycle VIII, denoting a significant contrast with prevalent FA5, FA6 and FA7 in the lower cycles. It consists of a structureless coarse to very coarse white to slightly red mosaic carnallite mixed with accessory zoned to clear halite crystals (Fig. 10A). The red carnallite forms localised patches in a prevalent mixed clear translucid carnallite and halite fabric.

In thin section, clear carnallite crystals form a mosaic arrangement of coarse birefringent porphyroblasts over 100 μm across, characterised by sharp extinction (Fig. 10B). They poikilotopically cement smaller zoned halite crystals that display sharp truncated boundaries. Carnallite sutures are mostly sharp and irregular, often marked by smaller clear euhedral halite sub-grains and insoluble linings. Carnallite is translucid because the crystals contain few iron oxides inclusions, often remotely dispersed (Fig. 10C). No replacement, pipes or epikarstic features were observed.

Unbedded coarse euhedral and clear carnallite crystals enclosing primary zoned halite have been described in recent lacustrine Qaidam evaporites in China as eodiagenetic void-filling cement resulting from the subsurface cooling of highly concentrated interstitial brine in the upper 14 m of a porous halite and muddy host, below the brine-sediment interface (Casas et al., 1990; Zhiqiang and Parnell, 1993).

The loss of iron oxide inclusions and the accumulation of residue at crystal junctions of the translucid carnallite of FA8 suggest a displacive origin. Depositional zoned halite crystals were partially dissolved because of a newly intrusive brine saturated with respect to carnallite. Carnallite crystals probably formed by direct precipitation on the pond floor, then were subsequently leached and removed downward into the inter-crystalline pore space of a halite substrate (Casas and Lowenstein, 1989).

The hydrological processes responsible for carnallite dissolution, *per descendum* migration, and recrystallisation into the halite host can occur either from interstitial brine with subsequent cooling in a phreatic zone (Casas and Lowenstein, 1989; Spencer et al., 1990; Casas et al., 1990; Zhiqiang and Parnell, 1993; Duan and Hu, 2001) or capillary evaporation in a vadose zone above the water table (Powers and Hassinger, 1985; Holt and Powers, 1990, 2011). An interstitial brine ponding to cooling mechanism is favoured to explain the formation of FA8 because no *syn*-sedimentary dissolution pipes, pits or karstified surface, subaerial exposures with clastics, breccia and massive insoluble residue layers have been observed.

6.9. FA9: coarse to fine-grained bedded sylvinite

The sylvinitic rocks largely occur in the uppermost part of the Loémé Fm as flat-bedded strata ranging from several metres up to 50 m thick,

Fig. 9. Photographs of FA7 facies and micro-facies. A) Microcrystalline red carnallite cumulates and interbedded halite laminites (K1 well, 647.47 m, cycle IV). B) and C) Granoblastic equigranular fine-grained red carnallite texture, respectively under natural and polarized light (K55 well, 675.67 m, Top cycle IV). D) and E) Details of tinted fine-grained carnallite cumulates of B) (natural light). F) Example of white translucid to red medium-grained carnallite interlayered with red carnallitic laminites (natural light) (K55 well, 675.67 m, Top cycle IV). G) Detail of white to red medium-grained carnallite texture illustrated in F) (natural light).

in the vicinity of the anhydrite caprock (Fig. 3). Exposures in the Holle mine indicate that most of the sylvinite layers are horizontally stratified and lie unconformably on tilted carnallite-bearing beds of cycle IX, at the crests of anticlinal folds (Fig. 11). Isolated centimetre across carnallite lenses were also described entrapped into the sylvinite beds at Holle and Kola prospects (Pedley et al., 2016). FA9 consists of white faintly

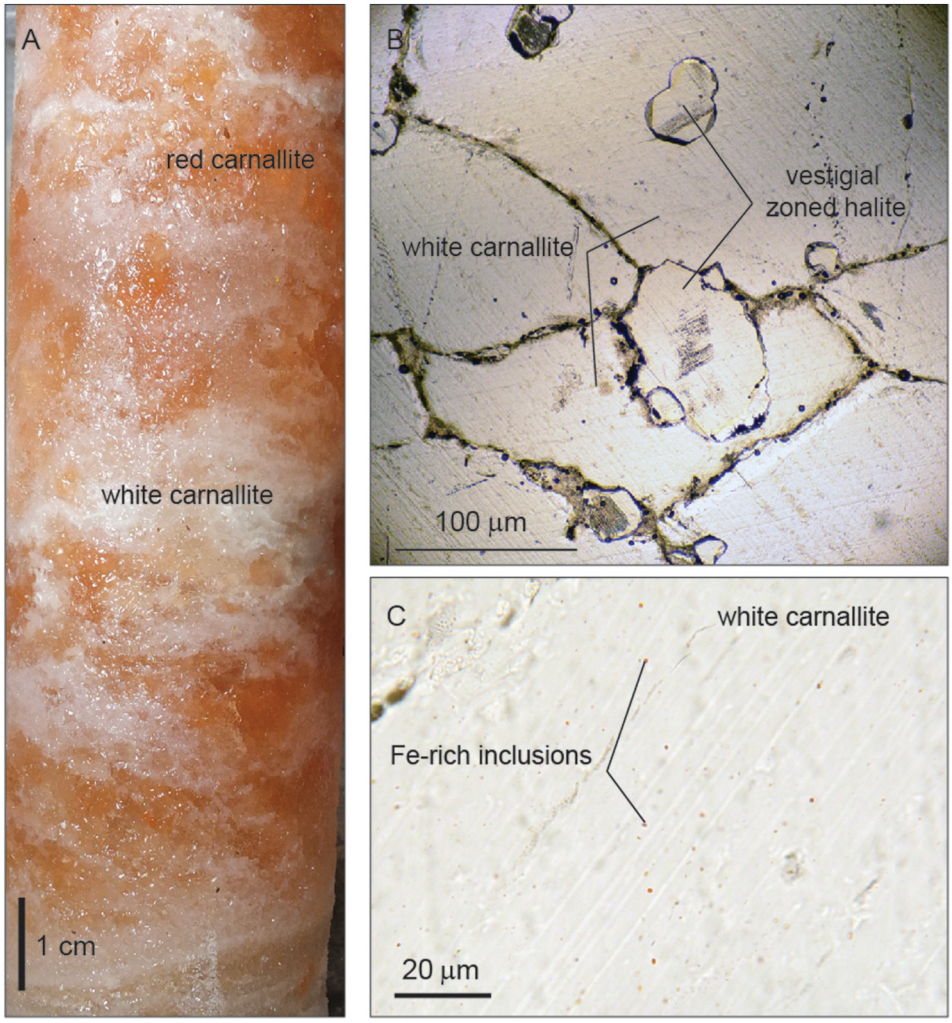

Fig. 10. Photographs of FA8 facies and micro-facies. A) Example of unbedded coarse-grained white to reddish carnallite fabrics. B) Granoblastic mosaic of translucid carnallite porphyroblasts and banded halite crystals. Note that, locally, carnallite poïkilotopically cements zoned halite. C) Remotely dispersed iron oxides inclusions with carnallite.

layered halite that grades upward into thin anhydritic seams and sharp-based massive sylvite (Fig. 12A, B, C). At bed scales, the sylvite may truncate or pass laterally into the carnallitic FA7 or FA6 along the down-verged anticline flanks. Locally, some pockets filled by centimetre-scale euhedral sylvite cubes are preserved underneath the unconformities.

Sylvite to sylvinitic micro-facies display a broad range of co-existing crystalline forms from translucid to lie-de-vin, red to blue euhedral cube aggregates and anhedral displacive spar (Fig. 13A, B, C). Displacive crystals form cements that commonly display randomly oriented iron-oxide inclusions. The crystals poikilotopically enclose smaller rectangular, hexagonal to polygonal euhedral crystals, as well as perfect cubes of clear translucid sylvite. The rims of the sylvitic sparry cement show curved, amoeboidal to crenulated shape, lined up by iron oxide concentrations.

When associated with carnallite, sylvite is typified by millimetre-sized cubes preferentially occurring along the crystalline cleavage planes, at grain boundaries, from crystal host centres, or even along solutional re-entrants (Fig. 13D). Locally, sylvite entirely replaces carnallite or euhedral halite crystals (Fig. 13E). The dull and white halite associated with anhydrite seams displays recrystallised interlocking texture with abundant residual dolomicritic mud at the sutural contacts of sparry crystals (Fig. 13F).

The erosional unconformity that separates folded carnallitic and massive sylvinite beds represents the last diagenetic front that accounts for the transformation of depositional carnallite into secondary sylvite. The horizontal beds of FA9 represent "pseudo-stratifications" resulting from the incremental dissolution and replacement of carnallite caused by the downward migration and leaching of a pervasive flat-lying phreatic water table. *In situ* recrystallised halite and sylvite occur at each down-stepping flushing episode, following the bedding of the dissolved primary halite-carnallite couplets. Horizontally layered sylvinite is described in the Oligocene evaporites of the Upper Rhine Graben in the north-east of France (Blanc-Valleron and Gannat, 1985; Blanc-Valleron, 1990) and in the Cretaceous Maha Sarakham Fm along the western margin of the Khorat Plateau in Thailand (El Tabakh et al., 1999; Warren, 2006). Both are preserved as conformable and correlative bottom-growth halite and sylvite beds without carnallite relics within subsiding syncline ponds, testifying of primary depositional deposits.

Residual anhydrite and insoluble minerals have accumulated at diagenetic halite-sylvite boundaries as a result of the complete leaching of impure carnallite that pushed the enclosed less soluble inclusions outwards. Dissolving fresh waters locally created small voids along or at the top of carnallitic beds in which secondary sylvite cubes could freely nucleate. The carnallite-sylvite replacement could be partial and operated along weakness zones of carnallite crystals (*i.e.* along cleavage planes or crystal boundaries) where sylvine cubes nucleated. Sylvine could also entirely replace euhedral halite zoned cubes. Similar relationships in the potash layers in the Prairie Fm of the Saskatchewan Basin are described by McIntosh and Wardlaw (1968).

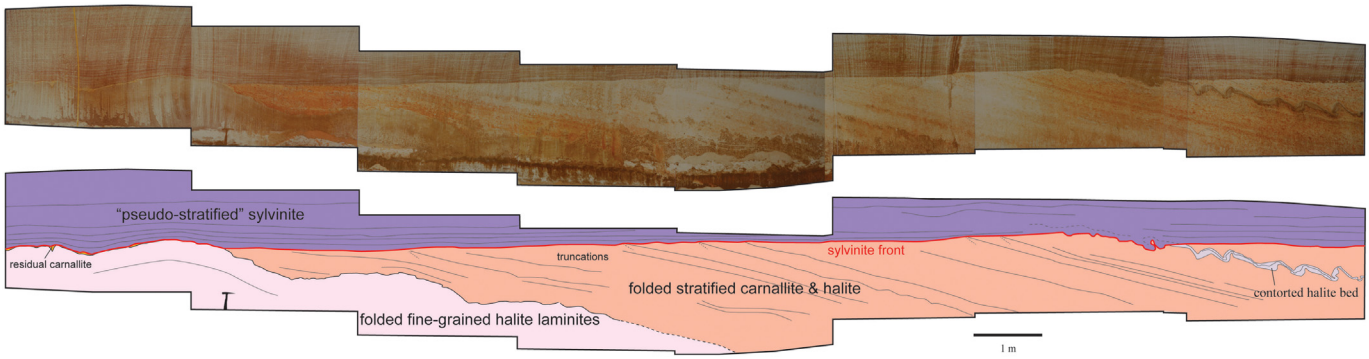

Fig. 11. Panoramic view of the carnallite – sylvinite transformation front of cycle IX at the vicinity of the K1 borehole within the Holle mine (Courtesy of the Kalivie Museum, photographs taken by J.-M. Schlund, 1976).

The transformation was complete where flushing was entirely pervasive, resulting in newly formed displacive tinted sylvite spar that grew in all directions as testified by the widespread crystalline distribution of iron oxides at crystal boundary. A last generation of secondary euhedral clear sylvine crystals grew freely into the sparry cement until the potassium saturation of the stagnant perched brine is depleted.

7. Bromine trace element variations

Bromine trace elements (Br) have the ability to incorporate chloride minerals when they crystallise from saline waters by replacement of Cl-ions by Br- (Garrett, 1970). With an ionic radius of 1.96 **Å**, it easily substitutes for chlorine (whose ionic radius is 1.81 **Å**) within the chloride salt lattice (Moretto, 1988). The concentration of Br in solid depositional salts is usually proportional to the Br concentration, composition and temperature of the evaporating parenthood brine (Valyashko, 1956; Braitsch and Herrmann, 1964; Holser, 1966), When the effects of trapped fluid inclusions, recrystallisation and replacement are eliminated (Moretto, 1988; Cathro et al., 1992), the bromine content is commonly employed for approaching the marine or non-marine origin of brine chemistry (Hardie, 1984; Rosell and Pueyo, 1997). It also represents an indicator for chloride saturation degree and, by extent, evaluate the relative palaeosalinity (Wardlaw and Schwerdtner, 1966). The use of shape analysis of bromine profiles usually helps in interpreting parenthood brine rhythmic fluctuations in time and identify diagenetic textures related to recycling or dissolution/recrystallisation events (Raup and Hite, 1978; Fontes et al., 1991; Hovorka et al., 1993; Risacher and Fritz, 2000).

The vertical distribution of the bromine content for the halite fraction varies between 80 and 700 ppm, with most of the values between 200 and 400 ppm from cycle II to IX (Fig. 14). The bromine content of carnallite varies between 1940 and 6230 ppm, with most values between 2000 and 4000 ppm.

The overall vertical evolution of bromine concentration for halite accounts for a long-term bromine curve that can be divided into medium-term bromine profiles that in turn are composed of stacked shorter term

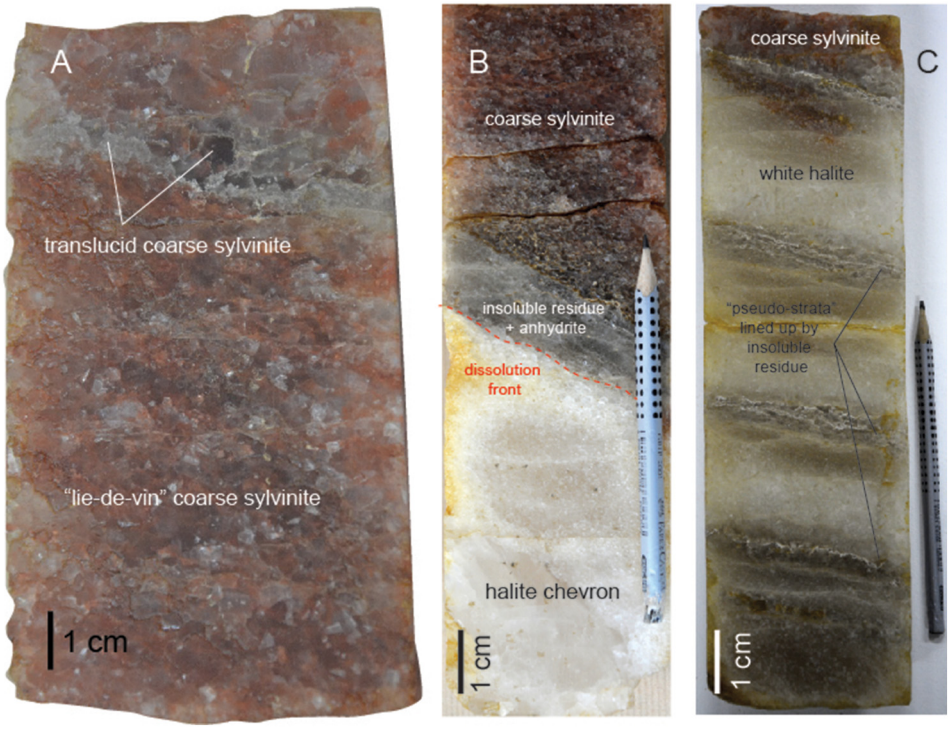

Fig. 12. Photographs of FA9 facies association. A) Reddish to "lie-de-vin" very coarse-grained sylvite (K1 well, 292 m, cycle IX). B) Detail of stratigraphic contact between white secondary halite and "lie-de-vin" secondary sylvine. Note the grey anhydrite seam at the halite-sylvite boundary (K1 well, 290 m, cycle IX). C) Details of flushed secondary halite of FA9 with thin disseminated anhydrite seams (K1 well, 293 m, cycle IX).

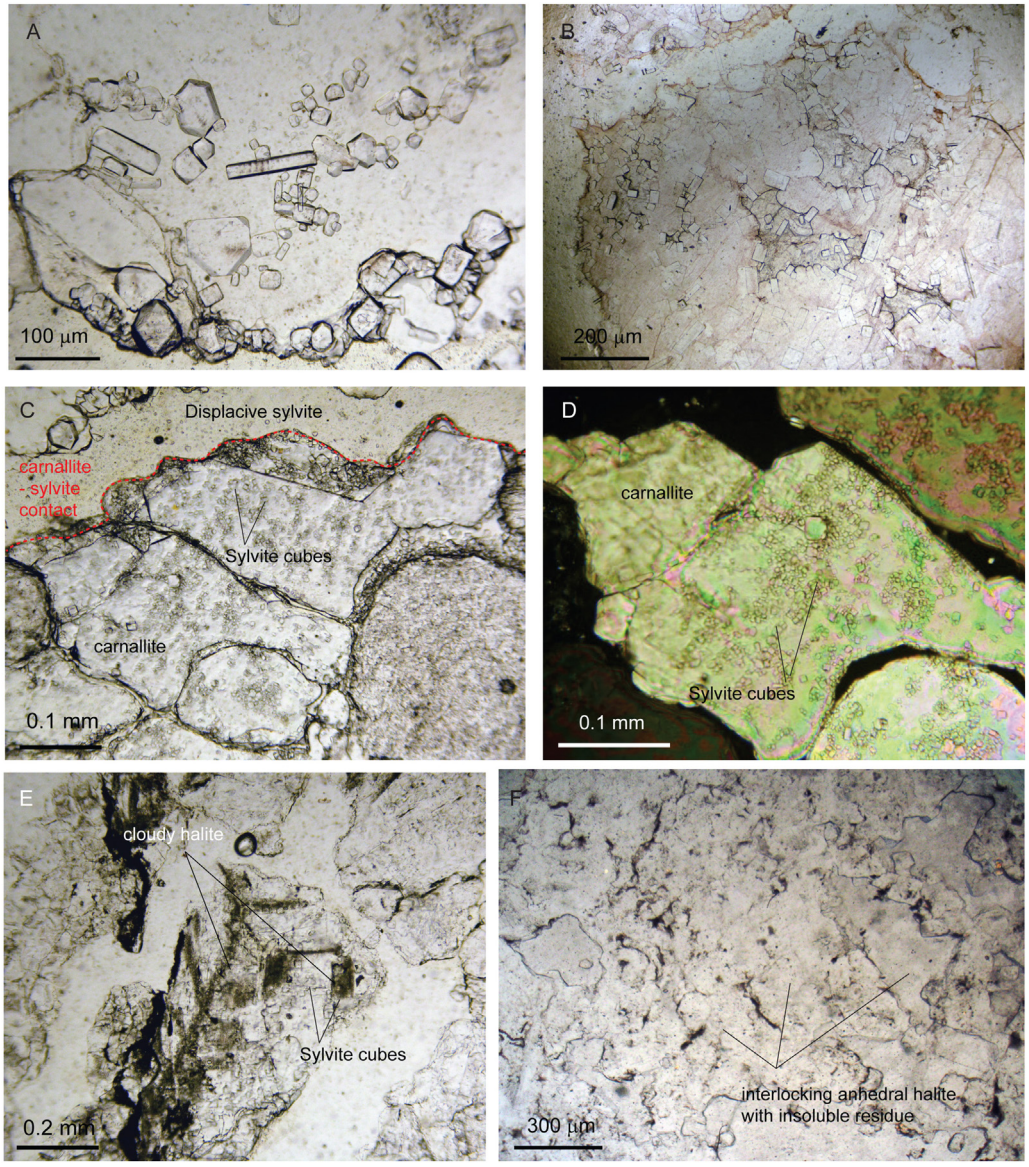

Fig. 13. Photographs of sylvinite FA9 micro-facies (K54 well, 336.41 m, cycle IX). A) Perfect euhedral clear sylvite crystals cemented by amoeboid displacive sylvite spar. B) Free-grown euhedral clear sylvite cubes and laths cemented by "lie-de-vin" displacive sylvite spar. C) Detail of carnallite-sylvite contact. Sylvite cubes progressively replace carnallite by nucleating along cleavage planes and peripheral boundary of nodular carnallite porphyroblasts. D) Detail of partial carnallite replacement by secondary sylvite along cleavage planes. E) Detail of gradual replacement of zoned halite cube by sylvite. F) Detail of interlocking anhedral recrystallised halite texture.

motifs. The long-term bromine content for the halite fraction increases from base cycle II to base cycle IX. It displays, however, a significant depletion in the upper part of cycle IX where sylvinite occurs. Likewise, the overall bromine concentration of carnallite increases from cycle II to the top of cycle VIII.

From cycle II to the top of cycle VI, the bromine concentration of halite progressively increases from 70 to 500 ppm (Fig. S1). The short-term patterns display asymmetrical bell-shapes, characterised by a short gradual decrease at the base of the MDPA cycles, followed by a thicker regular increase of bromide values. Carnallite shows similar medium-term rising trends, ranging from 2000 to 4000 ppm.

From cycle VII to cycle IX, the medium-term distribution of bromine concentration for both halite and carnallite increases with strong irregularities. The base of cycle VII is characterised by a significant shift of halite bromine content, followed by an irregular bell-shaped motif displaying high magnitude variations of bromine content. The cycle VIII also reveals a strong irregular bromine profile, starting with a basal negative shift followed by an upwards increase, which in turn is marked by a longer depletion. The vertical distribution of bromine concentration for carnallite shows a cylinder-shape profile standing around 3100 ppm in average at the top of cycle VII, whereas it presents further irregularities for cycle VIII ranging from 3500 to 6100 ppm.

The sylvinite of cycle IX shows bromine contents ranging from 520 to 1160 ppm (Fig. 14). As with cycle VIII, it is marked by a basal bromine depletion, followed by a subsequent rise that rapidly displays a newly funnel-shape motif. The recrystallised white halite of FA9 is characterised by lower bromine content with respect to primary halite of FA2 to FA4, ranging from 300 to 450 ppm (Fig. 13F). The trace elements composition of the sylvinite is consistent with the facies description of FA9, suggesting stratified alternation of recrystallised halite and sylvite separated by anhydrite seams (Fig. S2).

8. Discussion

8.1. Depositional facies model

Detailed examination of evaporites facies throughout cycles II to base IX of the Loémé Fm enabled us to define eight depositional facies

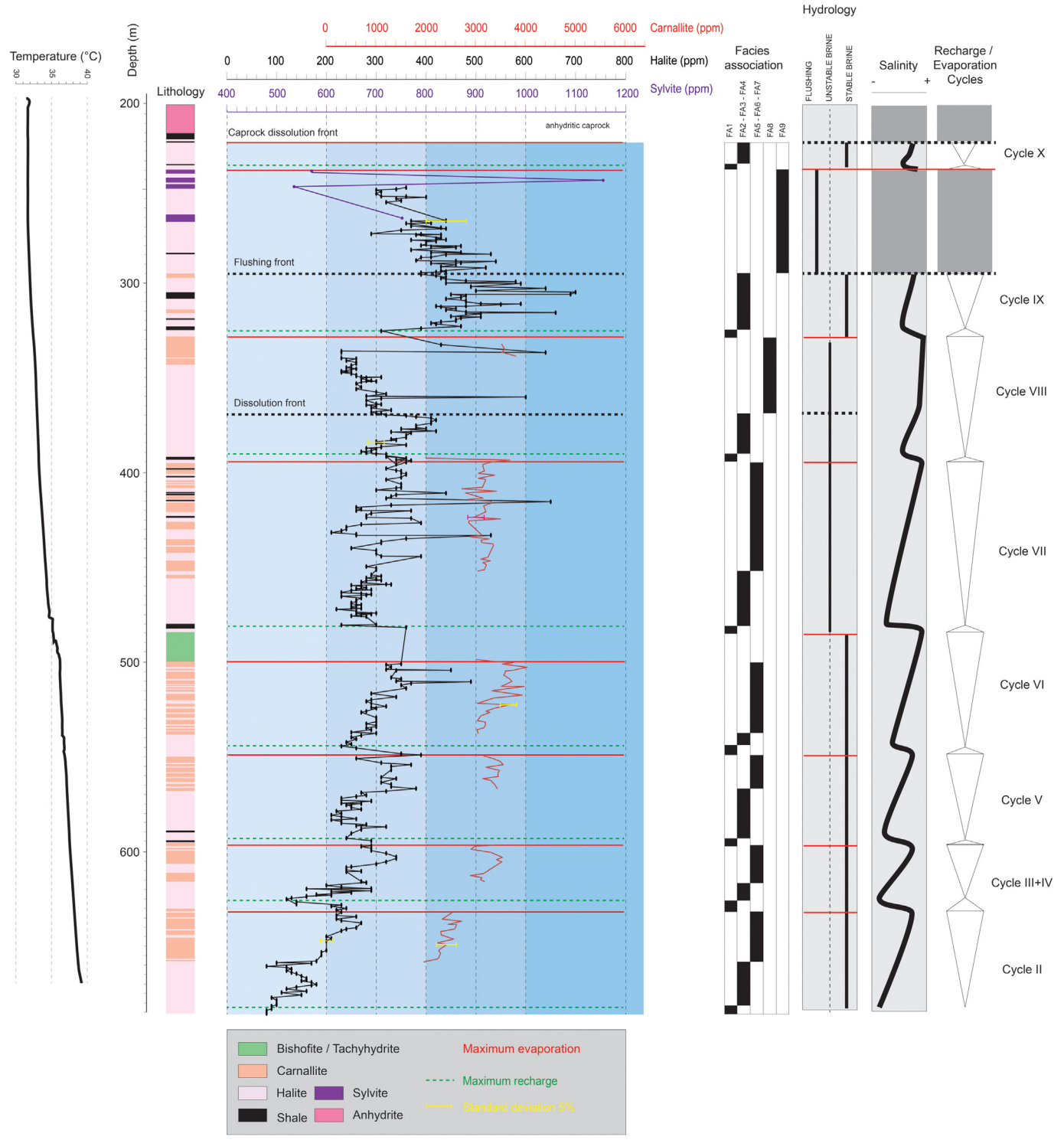

Fig. 14. Relationships between the bromine profiles, respectively calculated for halite, carnallite, bischofite and sylvite fraction, and the evolution of the interpreted hydrology and brine palaeo-salinity from cycle II to base cycle X, compiled from the K40 borehole. Note that sylvinitisation front appears at the base of cycle IX. A profile of borehole temperatures is also displayed in depth.

associations, named as FA1 to FA8, which successively respond to salinity, brine saturation and water level variations during recharge-to-evaporation cycles. We propose a depositional model that reconciles the spatial distribution of facies associations with respect to multi-stepped increasing brine saturation and shallowing (Fig. 15). A depositional sequence can be described as a series of hydrological stages as a response to decreasing water depth, characterised by a brine progressively saturated with respect to halite (stages 1 to 2) then carnallite (stages 3 to 4). The sequences II to VII show facies associations attributed to stages 1, 2 and 3, while the sequences VIII and IX reach the stage 4.

The differences between all facies associations reside in the preservation or absence of several features that account for the hydrological conditions under which evaporites had crystallised. To describe the

bathymetric zonation along a depositional profile at any stage of salinity and brine saturation, we focus on the following features:

1. Fluid inclusions banding in crystals that is usually driven by variations of crystallisation rates that relate to variations of halite saturation degree at brine-air interface or along shallow margins (Hardie et al., 1985; Roberts and Spencer, 1995; Benison and Goldstein, 1999, 2000). Their occurrence indicate whether crystals (bottom-growth, cumulates) form in a water column that underwent daily temperature variations or not. Zoned crystals can be inherently related to thermally-influenced shallow environments, whereas clear crystals commonly precipitated in a deeper environment that inherently records less daily temperature contrast,
2. The grain-sizes of crystals testifying to (i) the brine saturation degree (Kiro et al., 2015; Pueyo et al., 2017; Sirota et al., 2017) and (ii) the parent brine stability and crystallisation duration,
3. Dissolution features or surfaces as diagnostic of periods of thermally-driven brine under-saturation, freshening or emergence (Shearman, 1970; Casas and Lowenstein, 1989; Schubel and Lowenstein, 1997; Hovorka et al., 2007; Sirota et al., 2020),
4. Laminated or enclosed carbonate, sulphate and detrital mud deposited from terrigenous inflows or brine recharges (Lowenstein and Hardie, 1985; Schubel and Lowenstein, 1997),
5. The net thickness ratio between bottom-growth layers and laminites which indirectly accounts for the precipitation rate and salt accumulation interruption (Hovorka et al., 2007; Sirota et al., 2020), and
6. Sedimentary structures preservation (Weiler et al., 1974; Gornitz and Schreiber, 1981; Schreiber and El Tabakh, 2000).

During the Stage 1, bottom-growth halite may have developed at any depth of the coastal domain as brine initially became saturated with respect to halite. Fluid inclusions were entrapped in skeletal halite chevrons and hoppers that form in shallow brines or at the brine-air surface as daily temperatures varied. Clear halite cement and planar dissolution surfaces were common along shallow margins because of freshening (FA3b), compared to deeper settings where the impact of under-saturated brine was less effective (FA3a and FA2) (Shearman, 1970; Lowenstein and Hardie, 1985; Schreiber, 1988; Sirota et al., 2016, 2017, 2020). Continental water inflows and subsequent ephemeral brine under-saturation also caused the deposition of thin dolomicrite, anhydrite and detrital mud layers in shallow environments (FA3a and FA3b). With increased water depth, clear chevrons and zoned cumulates freely grew and accumulated without interruption by detrital mud, with brine being protected from continental influxes (FA2).

During the Stage 2, the halite saturation reached its maximum because of continuing evaporation. As brine level fell with salinity increase, zoned cumulates increased relative to coarsely bottom-growth halite. The cumulates crystal size of FA4 is in average less than the ones of FA3, traducing a higher degree of halite saturation in comparison with the Stage 1 (Sirota et al., 2017). In shallow settings, continental inflows caused ephemeral brine stratification, resulting in halite laminites with frequent planar dissolution surfaces and enclosed polyhedral dolomite and anhydrite inclusions (FA4b). The freshening impeded the full crystallisation of cumulates, and these cumulates underwent partial dissolution and lead to dolomicrite and anhydrite draping at the pond floor. Fair-weather waves reworking also indicates subaqueous shallow conditions (Schreiber and El Tabakh, 2000). Deeper domains were sheltered from freshening episodes and brine agitation, leading to the accumulation of flat and conformable pure halite laminites (FA4a).

When the parent brine reaches carnallite saturation during the Stage 3, dense and interstitial brine ponding occurred first, inducing the crystallisation of carnallite nodules into still porous laminated halite host. With increasing salinity, carnallite bottom-growth crystals freely nucleated at pond floor in subaqueous residual brine (FA5). It is still unclear why some bedded bottom-nucleated carnallite textures remained intact and others evolved into nodular "brecchoid" fabrics during burial (F6).

During the Stage 4, free nucleation of carnallite "rain" and subsequent deposition of laminites (FA7) prevailed because of a residual brine saturation that reaches its maximum (as with the halite formed during Stage 2). Because the brine was so concentrated, freshening induces halite laminites interbedded with fine-grained carnallite, instead of dolomicrite or anhydrite drapes. Brine ponding operated near the sediment-brine interface along shores where the water table dropped sufficiently. Subaqueous dissolution of the halite host and downwards migration of carnallite-saturated interstitial brine led to the formation of FA8. The coexistence of altered zoned halite crystals cemented by clear translucid carnallite indicates very shallow water conditions.

Early diagenesis linked to shallow burial affected primary textures but it had a limited effect on halite and fine-grained carnallite, in which compaction-derived pressure-dissolution led to minor solutional sutures and inter-crystalline clear crystals. Because of its rheological weakness caused by inherent hydromorphic properties (Koeler et al., 1990; Koeler, 1997; Urai et al., 2008), the coarse bottom-growth carnallite underwent further physical changes during burial, resulting in bedded nodular fabrics.

By comparison with the others salt basin of the South Atlantic margin, sulphates deposits remain relatively poorly represented though the Loémé Fm of Congo, only typified by anhydrite caprock, millimetre-thick seams and minute inclusions into halite. In the southern Santos Basin and the northern Serguipe Basin of Brazil, centimetre to metre thick interbedded depositional anhydrite and dolomitic carbonates alternate with halite (Borchert, 1977; Szatmari et al., 1979, 2021; De Freitas, 2006; Rodriguez et al., 2017). In contrast, along the onshore Namibe Basin of South Angola, exposed secondary gypsum of the Bambata Fm is interpreted as represented the final residual product of fractional dissolution and recrystallisation of the halite mass but not depositional textures (Gindre-Chanu et al., 2016). This variation of occurrence, thickness and origin of depositional sulphates along strike either reveals a palaeogeographic segmentation of the Aptian salt giant with a hydrological disconnection of sub-basins (Davison, 2007) or indicates a position nearby or away from seawater entry points (Rodriguez et al., 2017; Szatmari et al., 2021). A hydrological remoteness of the western African salt basins from recharge points can be proposed to explain the deficiency of sulphates deposits, while the percolation of seawater through mafic rocks of the southern proto-Rio Grande Rise – Walvis Ridge barrier would have favoured their deposition along shallow highs of the Brazilian salt basins as suggested by Nunn and Harris (2007) and Szatmari et al. (2021).

8.2. Palaeo-salinity evolution of Mid to Upper Aptian brine

The South Atlantic Mid to Upper Aptian Sea counts among the "$CaCl_2$" seas characterised by a Ca-rich and SO_4^{2-}-poor parenthood brine composition (Hardie, 1996; Lowenstein et al., 2001; 2003). Such enrichment into Ca^{2+} and depletion in SO_4^{2-} are consistent with the composition of fluid inclusions performed in zoned halite of the Loémé Fm. of Congo from the cycles I to X and the Muribeca Fm in the onshore Sergipe basin of Brazil (Timofeeff et al., 2006). They are interpreted as resulting from high influxes of mid-ocean hydrothermal brine enriched in $CaCl_2$ (Hardie, 1990, 1996) during which a rapid sea-floor spreading associated with basalt serpentinisation had played a significant role (Warren, 2006; Debure et al., 2019). Although the Ca, Cl and SiO_2 enriched hydrothermal influxes largely intend to brine palaeosalinity, the bromine is further known as being related to fresh or marine waters rather than mid-ocean ridge brines (Hardie, 1990). As previously quoted, the percolation of sea water through volcanic barrier also favours calcium incomes into the parent brine (Nunn and Harris, 2007).

The fact that bromine ions do not form separate minerals during brine concentration but substitute with Cl^- ions of chlorides allows us to predict indirectly brine saturation degree as it also remains straightforwardly related to the calcium concentration that intends to maintain

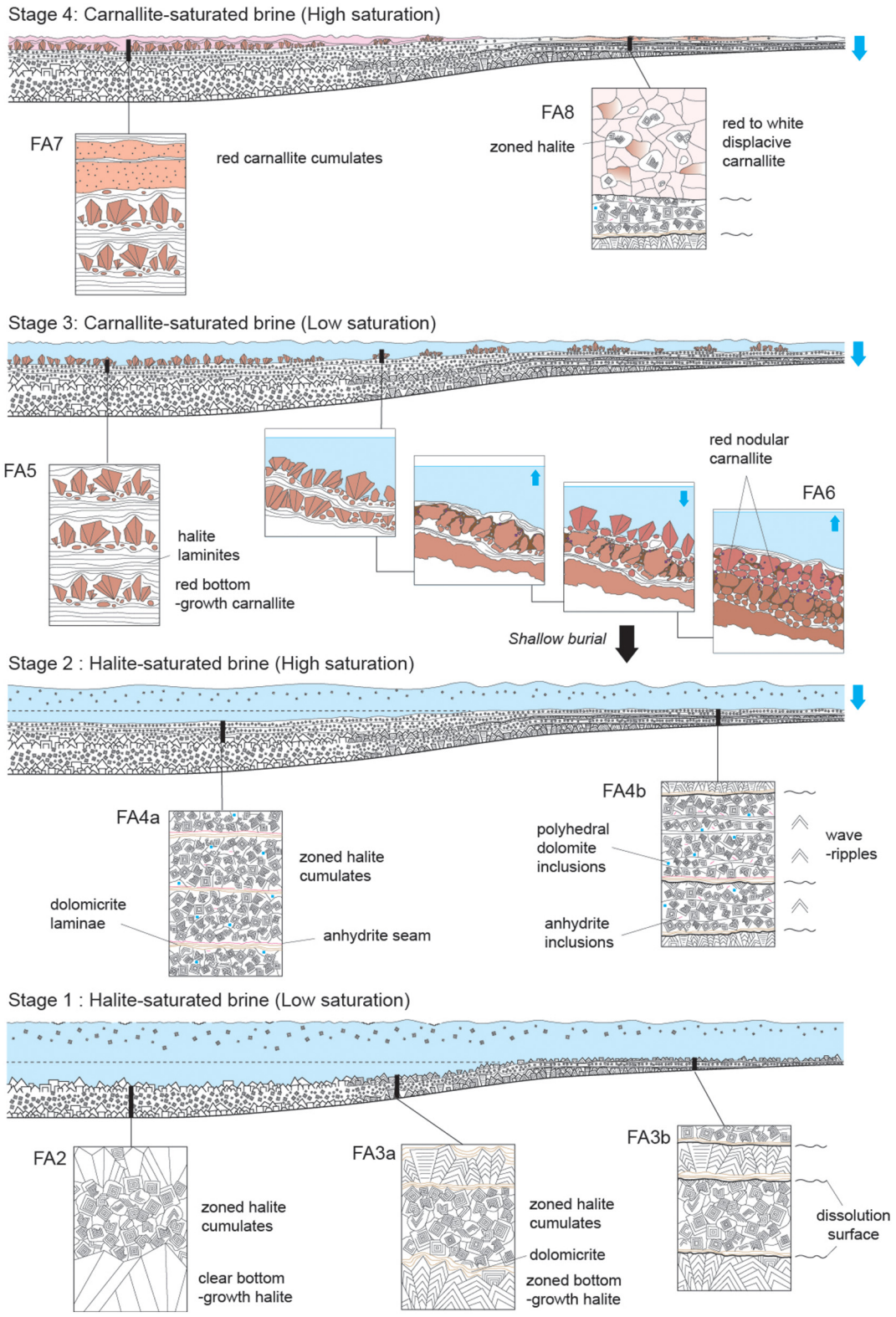

Fig. 15. Depositional model displaying spatial and lateral distribution of halite and carnallite-prone facies associations FA2 to FA8, with respect to each parent brine saturation stages and salinity increase.

a high Br partition coefficient during evaporites deposition (Siemann, 2003). A typical recharge-saturation sequence of potash-bearing evaporites deposited in subaqueous saturated brine is expected to impart a bromine depletion followed by an upwards increase of concentrations (Holser, 1966; Braitsch, 1971; Raup and Hite, 1978).

Although the origin of the depositional brine is difficult to assess by relying only upon the bromine averaged concentrations from bulk rocks (Hardie, 1984; Moretto, 1988), the relative brine salinities can be determined when a calibration with evaporite fabrics is performed (Raup and Hite, 1978) and the brine composition is assumed to not have

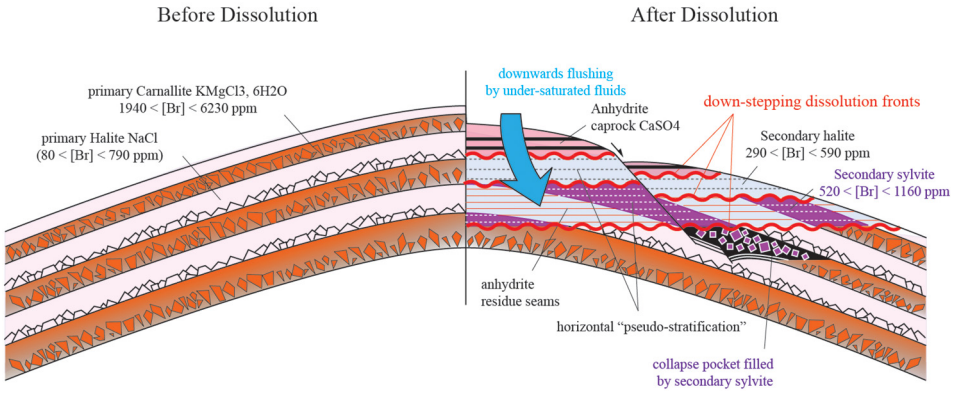

Fig. 16. Diagenetic model for the secondary sylvite formed at the top of folded structures of the Loémé Fm.

significantly changed (Wardlaw and Schwerdtner, 1966). The good correlation between short to long-term bromine profiles, shape parameters and facies sequences of the Loémé Fm enables us to use the vertical distribution of bromine to estimate the palaeo-salinity evolution of the parent brine from cycle II to base cycle IX.

Rhythmic short-term decrease-increase profiles of bromine in halite, characterised by funnel-to-bell graph shapes, form "ideal patterns" (*sensu* Holser, 1966) that can be respectively correlated with the recharge-saturation elementary depositional cycles II to VI. The short basal bromine depletion coincides with dilution episodes typified by FA1 shale deposits, while the subsequent increase in bromine concentration matches with brine saturation evidenced by the grading occurrence of halite prone FA2 to FA4 (Fig. S1). Carnallite occurs in the uppermost part of evaporation half-cycle, and it displays a slight positive increase of bromine content, indicating a progressive concentration of carnallite-saturated brine. The regular shape of bromine profiles indicate that the evaporites have precipitated under subaqueous stable brine conditions, less influenced by detrital mud.

Cycle VII displays a profile similar to the preceding cycles for halite, but the increase of bromine concentration related to saturation half-cycle is marked by irregular and serrated patterns, indicating shallow environments affected by surficial and rapid compositional brine changes (Raup and Hite, 1978). This is consistent with the frequent dolomicrite and shale laminae associated with halite and carnallite preserved in the saturation half-cycle (Fig. 14).

The bromine depletion of the uppermost part of cycle VIII is correlated with dissolved halite and clear displacive carnallite of FA8, interpreted as resulting from *syn*-depositional dissolution and brine ponding in a very shallow environment. Similar surficial dissolution and recrystallisation processes along recent shallow lacustrine carnallite-bearing salt flats characterised by bromine funnel-shape profiles have been observed in the intra-montane Qaidam basin of China (Casas et al., 1990; Duan and Hu, 2001).

The bromine profile of cycle IX indicates brine freshening at the base with FA1 occurrence, followed by an increasing saturation trend, characterised by FA2 to FA4 with abundant shaly and dolomicrite layers. The irregular shape of bromine variations indicates unstable shallow brine hydrology, influenced by frequent detrital inflows. The significant bromine depletion at the stratigraphical level of sylvinite FA9 in the uppermost part of cycle IX indicates a dissolution anomaly (Fig. 14).

Bromine concentrations of the Aptian evaporites preserved along the South Atlantic margin are among the highest values known for Cretaceous evaporites (Wardlaw, 1972; Wardlaw and Nicholls, 1972; El Tabakh et al., 1999). Relying upon the results of these studies, three points are proposed to explain such high values and evolution:

(1) The petrographical analysis shows depositional textures with minor compaction-related clear halite and carnallite. Bromine values related to diagenetic clear halite are barely discernible (Cathro et al., 1992) or *a contrario* quite high (Wardlaw and Schwerdtner, 1966) in the total amount of bromine concentrations measured from bulk rocks. Moreover, the bromine trapped in primary fluid inclusions within halite could have also largely intended in the high average content (Moretto, 1988).
(2) The analysis of facies and bromine profiles at Holle indicate a brine shallowing upwards trend from cycles II to base IX. Syn-depositional dissolution of marginal facies, especially bromine-enriched halite and carnallite, becomes prominent as the pond shallows, causing a release of substantial secondary bromine into the parent brine by recycling (see Fontes et al., 1991).
(3) The recharges at the beginning of depositional cycles were probably insufficient to lower the Br contents (and thus of the salinity) of the parent-brine back to normal levels, such as the long-term bromine content keep increased. This suggests the progressive closure and confinement of the evaporative salt basin from open marine inflows at least up to cycle IX, leading to a generally increasing Br content through the sequence.
(4) As previously quoted, an excess of calcium cations into the parent brine favours bromine incorporation into chlorides evaporites by maintaining a high Br partition coefficient (Siemann, 2003). If we postulate that Ca-rich hydrothermal influxes are continuously maintained during the evaporites precipitation of the Loémé Fm from the cycles II to IX, very high bromine concentrations in halite and $MgSO_4$-poor potash are expected.

The variations of bromine concentrations can be used as a proxy for the palaeosalinity evolution but do not enable to know whether the parenthood brine saturation and palaeosalinity variations are related to recharge- net evaporation sequences or hydrothermal pulses.

8.3. Diagenetic model of secondary sylvinite

Sylvinite can form by direct precipitation from depositional saturated brine (Blanc-Valleron, 1990; Lowenstein and Spencer, 1990; Cendón et al., 1998), as pedogenetic potash in a hyper-arid climate (Eckardt and Spiro, 1999; Eckardt et al., 2001; Gindre-Chanu et al., 2016), by syndepositional replacement of carnallite during freshening events (Szatmari et al., 2021), by syn-tectonic recycling of carnallite (El Tabakh et al., 1999; Krupp, 2005; Warren, 2006), by incongruent dissolution of carnallite during burial (called "metamorphic" sylvite) (Rosell Ortiz and Ortí Cabo, 1981-1982; Koeler et al., 1990; Koeler, 1997), during telogenetic flushing of carnallite by downward pervasive under-saturated connate waters (Wardlaw, 1968; Pedley et al., 2016) or by transformation of bischofite by released potassium and magnesium-rich brines (Pedley et al., 2016).

In onshore Congo, the structural position of the sylvinite as discordant layers along anticlinal crest and the petrographic textures support

an origin of sylvite involving a flushing of carnallite by under-saturated waters and illustrates in detail the conclusions of Pedley et al. (2016) and Van Der Klauw et al. (2019). The bromine values of sylvite ranging from 520 to 1160 ppm, are also consistent with a secondary origin because geochemical signatures for primary sylvite are known to be much higher (between 2890 and 2540 ppm) (Braitsch and Herrmann, 1964). The discrepancies between bromine content of carnallite and secondary sylvite are interpreted as resulting from a change of substitution coefficient between the solid and liquid phase when carnallite is dissolved by fresher waters and recrystallise into sylvite (Cheng et al., 2016). Because the carnallite dissolution rate is lower than sylvite nucleation, the volume of released bromine that substitutes into secondary sylvite is consequently low.

Post-depositional flushing can occur at any evolutionary stage of evaporite rocks, from their deposition, through burial and halokinesis and up to their final exhumation, leading to bromine anomalies that often yield inconsistency with conventional profiles. In the Ibura member of the counterpart Brazilian Sergipe Basin, a secondary sylvinite layer with Br content ranging from 830 to 1340 ppm (*i.e.* similar than in the Congo Basin; Wardlaw, 1972) was interpreted by Szatmari et al. (2021) as contemporaneous with depositional evaporites and formed by the decomposition of carnallite and bischofite after a marine flooding during the Lower Albian.

At Holle, the onset of the secondary sylvinite remains difficult to assess with precision. However, the existing geometrical relationships between horizontally bedded sylvinite and salt anticlines indicate that phreatic flushing was post-depositional and at least syn- to post-deformational. Pedley et al. (2016) show that most of large-wavelength antiforms and synforms along the stable domain of Congo resulted from the exhumation of the margin during the Oligocene and Miocene. However, flushing could have been initiated earlier, as local to regional unconformities observed between the Maastrichtian and Palaeogene indicate uplift episodes (Reyre, 1984).

Finally, structural, petrographic and Br contents in the Holle Mine lead to an updated diagenetic model of the sylvite formation in the Congo Basin (Fig. 16). This model emphasizes the unconformable position of sylvite and the spatial relationships of the different primary *versus* secondary petrographic textures of halite, carnallite and sylvite.

It also highlights the pseudo-layering formed by the down-stepping migration of incremental dissolution fronts sourced from the infiltrated phreatic to connate waters, and by the subsequent replacement of carnallite into secondary sylvite that crystallises *in situ* by following the horizontal water table. Pedley et al. (2016) invoked leaching of depositional carnallite by the progressive invasion of flushing phreatic waters at the heads of folded structures to explain the perched sylvinite. Gypsum dehydration from the post-salt fractured Albian limestones could have also caused the release of saline waters during shallow burial that would have penetrated the top of the Loémé evaporites (SRK Consulting, 2012). The sylvinite is independent of its stratigraphic position and is mostly located at the top of anticline or along their flanks, formed in the cycles VIII, IX and X (Pedley et al., 2016; Van Der Klauw et al., 2019). The sylvinite beds display horizontal “pseudo-bedding” and unconformably truncate the top of salt anticlines in the style of a sharp-based caprock (Figs. 11, S2). Pseudo-layering is here interpreted as having formed by the down-stepping migration of incremental dissolution fronts sourced from the infiltrated phreatic to connate waters, and by the subsequent replacement of carnallite into secondary sylvite that crystallises *in situ* by following the horizontal water table. At each flushing step, secondary sylvite and halite respectively replace alternated depositional carnallite and halite beds, leaving behind less soluble anhydrite seams. Leaching is indicated by the dilution of iron oxides that preferentially concentrate at the periphery of sylvite spars. In response to water loss through the carnallite-sylvite transformation, the volume of evaporites rock reduces, creating fractures, voids and local collapse.

8.4. Comparison between the Congolese and Brazilian Aptian evaporites

Horizontally bedded MgSO4-poor potash bearing evaporites is up to 500 m-thick are also preserved along the Brazilian margin, typified by the Aptian Ibura member of the Muribeca Fm in the onshore Sergipe Basin (Wardlaw, 1972; Wardlaw and Nicholls, 1972; Borchert, 1977; Szatmari et al., 1979, 2009, 2021; Davison, 2007).

Although thin stringers of anhydrite and dolomitic carbonates are frequently intercalated, the lithological composition of the Ibura member is strikingly similar to the Loémé Fm. Nine correlative depositional sequences are interpreted as solar evaporation driven cycles, influenced by hydrothermal activity, leading to the accumulation of halite-carnallite- tachyhydrite/bischofite suites (Szatmari et al., 2021).

Bottom-nucleated coarse-grained, nodular and microcrystalline carnallite fabrics are largely reported in the lower cycles which also display a progressive increase of stacked carnallite and tachyhydrite proportions with respect to halite (Wardlaw, 1972; Szatmari et al., 1979, 2009, 2021). Such carnallite fabrics show strong similarities with depositional textures respectively attributed to facies associations FA5, FA6 and FA7 observed from the cycles I to VI of the Loémé Fm, which also display a potash thickening upwards pattern.

Additionally, bromine trace elements values in both halite and carnallite bulk fractions rise upward from the cycles I to VII in the Sergipe Basin (Wardlaw, 1972), with contents respectively ranging from 100 to 700 ppm for halite and from 2000 to 7000 ppm for carnallite (Wardlaw and Nicholls, 1972). Such bromine values ranges and profiles are similar to the ones evidenced in Congo from the cycles I to VI, suggesting progressive brine salinity increase with a saturation reaching magnesium chloride potash all over the northern segment of the South Atlantic.

In the Sergipe Basin, the upper VII to IX cycles rest unconformably on the lower cycles and further record Mg-chloride-poor potash (sylvite), sulphate and halite (Szatmari et al., 2021). The unconformity is interpreted as a regional dissolution surface resulting from a North Atlantic sea water ingression that caused a drastic change of brine composition with respect to the lower cycles. Although no megaregional erosion was noticed within the Loémé Fm, a shift of brine composition can be fairly deduced from the cycles X and XI characterised by a significant decrease of carnallite proportion and the first record of depositional sulphate beds (Fig. 2). Accordingly, while the lower cycles I to VI both in Congo and Sergipe basins do not support a conclusion about a progressive brine salinity increase due to a likely palaeogeographic confinement, the upper cycles testify to more diluted brine resulting from the return of less saline and opened marine conditions.

9. Conclusions

-1 The subsurface evaporites of the Aptian Loémé Fm along the stable structural domain of onshore Congo are composed of slightly folded to horizontally well-stratified depositional halite (NaCl) interbedded with Mg-poor potash. The Mg-poor potash includes carnallite ($KMgCl_3$, $6H_2O$), bischofite ($MgCl_2$) mixed with tachyhydrite ($CaCl_2$,$2MgCl_2$, $12H_2O$) and secondary sylvite (KCl). The regional stratigraphy accounts for eleven correlative depositional sequences. Each sequence corresponds to a recharge-to-evaporation cycles typified by a gradual suite of facies made up of organic shale - halite - carnallite deposits, some of which punctuated by a bischofite-tachyhydrite end-member.

-2 Eight distinct halite and carnallite-prone facies associations, named FA1 to FA8, were interpreted using such descriptive parameters as fluid inclusions banding, grain-size, dissolution features, detrital sediments, minute inclusions and sedimentary structures occurrence. Based on the distribution of facies associations, a depositional model is proposed that explains salinity, brine saturation and palaeo-depth during evaporation half-cycles. Early burial diagenesis had only limited effect on the depositional textures, leading to minor compaction-driven surficial

dissolution of crystals and the formation of inter-crystalline clear incipient grains into finely crystalline halite and carnallite laminites. The evaporites formed from ponding of subaqueous shallow brines to interstitial brine from cycle II to the top of Cycle VIII, indicating a general shallowing upwards trend.

-3 Bromine trace element concentrations were measured from bulk evaporites for halite and carnallite fractions from cycle II to IX. The average bromine contents are the highest known worldwide for Cretaceous evaporites. This can be explained (1) because the bromine values were measured from bulk textures in which parent fluid inclusions are also incorporated, (2) because bromine was released from the *syn*-depositional recycling of very shallow halite and carnallite fabrics. An analysis of bromine profile shape and regularity reveals a progressive palaeo-salinity increase of the parent brine, which is consistent with the shallowing upwards sequence observed for cycle II to base IX. Such salinity increase might indicate a gradual confinement of the salt basin along the northern segment of the South Atlantic Ocean, an excess of saline elements inflow from hydrothermal vents, or a combination of both.

-4 The secondary sylvinite is independent of its stratigraphic position and is located at the top or along anticline flanks affecting cycles VIII, IX and X. It displays horizontal "pseudo-stratification" that lays unconformably at the top of salt anticlines in the manner of a sharp-based caprock. The sylvite has progressively replaced the depositional carnallite along crystal borders and cleavage planes prior to their complete cannibalisation. Downstepping incremental dissolutions sourced by pervasive phreatic to connate waters resulted in the flushing and transformation of depositional carnallite – halite into secondary sylvite – halite. Bromine concentrations confirm a diagenetic origin. Although the stratigraphic relationships at the crests of antiforms revealed it is post-depositional., the timing of sylvinite formation remains uncertain. We suggest that the post-salt phreatic to connate less saline waters invaded the uppermost Loémé Fm during the Upper Cretaceous, when folding deformation probably initiated.

-5 Similar depositional textures of halite and carnallite were observed in the lower cycles of the Aptian Ibura evaporites member in the counter-part Sergipe Basin in the northern part of the Brazilian margin. Additionally, a progressive rise of bromine trace elements concentrations, together with a carnallite to tachyhydrite proportion increase, also suggest a progressive palaeo-salinity increase of the mother brine all over the northern segment of South Atlantic. The sylvite formation of the Sergipe Basin differs from the one in Congo because it resulted from the syn-depositional carnallite/tachyhydrite dissociation due to a regional marine water ingression.

Supplementary data to this article can be found online at https://doi.org/10.1016/j.sedgeo.2021.106038.

Declaration of competing interest

The authors declare that they have no known competing financial interests or personal relationships that could have appeared to influence the work reported in this paper.

Acknowledgements

This study has benefited from data acquired by the Mines de Potasse d'Alsace (MDPA) that are archived by the Kalivie Museum located in Wittelsheim (France). All contributors sincerely thank TOTALENERGIES for the financial support, and Prof. Olga Otero and Paulo Brito from the University of Poitier for identifying the fish species. The authors are grateful to David W. Peacock, Dennis Powers and an anonymous reviewer for their careful reviews of the manuscript.

References

B.R.G.M, 1982. Carte de planification de ressources en eau Gabon-Congo. Comité interafricain d'études hydrauliques, B.R.G.M., Orléans (126 pp.).
Bate, R.H., 1999. Non-marine ostracod assemblages of the pre-salt rifts basins of west Africa and their role on sequence stratigraphy. In: Cameron, N.R., Bate, R.H., Clure, V.S. (Eds.), The Oil and Gas Habitats of the South Atlantic. Geological Society of London153. Special Publication, London, pp. 283–292.
Bate, R.H., Cameron, N., Brandao, M.G.P., 2001. Lower Cretaceous pre-salt stratigraphy of the Kwanza basin. Newsletters on Stratigraphy 38, 117–127.
Belmonte, Y., Hirtz, P., Wenger, R., 1965. The salt basins of the Gabon and the Congo (Brazzaville). Salt basins around Africa. Inst. Petroleum, London, pp. 55–74.
Benison, K.T., Goldstein, R.H., 1999. Permian palaeoclimate data from fluid inclusions in halite. Chemical Geology 154, 113–132.
Benison, K.T., Goldstein, R.H., 2000. Sedimentology of ancient saline pans: an example from the Permian Opeche Shale, Williston Basin, North Dakota. Journal of Sedimentary Research 70, 159–169.
Blanc-Valleron, M.-M., 1990. Les formations paléogènes évaporitiques du bassin potassique de Mulhouse et des bassins plus septentrionaux d'Alsace. (Ph.D. Thesis) Université Louis Pasteur, Strasbourg, p. 350.
Blanc-Valleron, M.-M., Gannat, E., 1985. Cartographie de subsurface du Salifère Supérieur du Bassin potassique de Mulhouse. Bulletin de la Societe Geologique de France 8, 823–836.
Borchert, H., 1977. On the formation of Lower Cretaceous potassium salts and tachyhydrite in the Sergipe basin (Brazil) with some remarks on similar occurrences in West Africa (Gabon, Angola, etc.). In: Klemm, D.D., Schneider, H.-J. (Eds.), Time and Strata-bound Ore Deposits. Springer-Verlag, Berlin, pp. 94–111.
Braccini, E., Denison, N., Scheevel, J.R., Jeronimo, P., Orsolini, P., Barletta, V., 1997. A revised chrono-lithostratigraphic framework for the pre-salt (lower Cretaceous) in Cabinda, Angola. Bulletin des Centres de Recherche Elf Exploration Production 21, 125–151.
Braitsch, O., 1971. Salt Deposits. Their Origin and Composition. Springer, Berlin, pp. 1–297.
Braitsch, O., Herrmann, A.G., 1964. Zur Geochemie des Broms in salinaren Teil II:Die Bildungstemperaturen primrer Sylvin- und Carnallit-Gesteine. Geochimica et Cosmochimica Acta 28, 1081–1109.
Brink, A.H., 1974. Petroleum Geology of Gabon Basin. American Association of Petroleum Geologists Bulletin 58, 216–235.
Caron, M., 1978. Cretaceous Planktonic Foraminifers from DSDP Leg 40, Southeastern Atlantic Ocean. Initial Reports of the Deep Sea Drilling Project 40, 651–678.
Casas, E., Lowenstein, T.K., 1989. Diagenesis of saline pan halite: comparison of petrographic features of modern, Quaternary and Permian halites. Journal of Sedimentary Petrology 59, 724–739.
Casas, E., Lowenstein, T.K., Spencer, R.J., Pengxi, Z., 1990. Carnallite mineralization in the nonmarine Qaidam Basin, China. Evidence for the early diagenetic origin of potash evaporites. Journal of Sedimentary Petrology 62, 881–898.
Cathro, D.L., Warren, J.K., Williams, G.E., 1992. Halite saltern in the Canning Basin, Western Australia: a sedimentological analysis of drill core from the Ordovician-Silurian Mallowa Salt. Sedimentology 39, 983–1002.
Cendón, D.I., Ayora, C., Pueyo, J.J., 1998. The origin of barren bodies in the Subiza potash deposit, Navarra, Spain: implications for sylvite formation. Journal of Sedimentary Research 68, 43–52.
Chaboureau, A.-C., Donnadieu, Y., Sepuichre, P., Robin, C., Guillocheau, F., Rohais, S., 2012. The Aptian evaporites of the South Atlantic: a climatic paradox. Climate of the Past Discussion 8, 121–144.
Cheng, H.D., Ma, H.Z., Hai, Q.Y., Zhang, Z.H., Xu, L.M., Ran, G.F., 2016. Model for the decomposition of carnallite in aqueous solution. International Journal of Mineral Processing 139, 36–42.
Cheng, H., Hai, Q., Li, J., Song, J., Ma, X., 2019. The sensitivity of temperature to tachyhydrite formation: evidence from evaporation experiments of simulated brines based on compositions of fluid inclusions in halite. Geofluids 2019, 1–16.
Coterill, K., Tari, G.C., Molnar, J., Ashton, P.R., 2002. Comparison of depositional sequences and tectonic styles among the West African deepwater frontiers of western Ivory Coast, southern Equatorial Guinea, and northern Namibia. The Leading Edge 21, 1103–1111.
Davison, I., 2007. Geology and tectonics of the South Atlantic Brazilian salt basins. In: Ries, A. C., Butler, R. W. H., Graham, R. H. (Eds), Deformation of the Continental Crust: the Legacy of Mike Coward. Geological Society, London, Special Publications 272, 345–359.
De Freitas, R.T.J., 2006. Ciclos deposicionais evaporiticos da basia de Santos: Una analise cilco-estrafica a parti de dados de 2 pocos de traços de sismica. (Ph.D. thesis) Universidade Federal do Rio Grande do Sul, Porto Alegre, Brazil (201 pp.).
De Ruiter, P.A.C., 1979. The Gabon and Congo Basins Salt deposits. Economic Geology 74, 419–431.
Debure, M., Lassin, A., Marty, N.C., Claret, F., Virgone, A., Calassou, S., Gaucher, E.C., 2019. Thermodynamic evidence of giant salt deposit formation by serpentization: an alternative mechanism to solar evaporation. Scientific Reports 9, 1–10.
Delhaye-Prat, V., Dupont, G., Buratti, N., Moron, J.M., Esnault, J., Perrichot, V., Garel, S., Callec, Y., Dal, J.-A., 2016. The Vembo shales (Republic of the Congo): New insights on the transition from lacustrine to marine settings for the South Atlantic. 35th IGC conference, Cape Town.
Dellwig, L.F., Evans, R., 1969. Depositional Processes in Salina Salt of Michigan, Ohio and New York. American Association of Petroleum Geologists Bulletin 53, 1–3.
Dias, J.L., 2005. Tectônica, estratigrafia e sedimentação no andar Aptiano da margem leste Brasileira. Boletim de Geociencias da Petrobras 13, 7–25.
Duan, Z., Hu, W., 2001. The accumulation of potash in a continentl basin: the example of the Qarhan Saline Lake, Qaidam Basin, West China. European Journal of Mineralogy 13, 1223–1233.

Eckardt, F.D., Spiro, B., 1999. The origin of sulphur in gypsum and dissolved sulphate in the Central Namib Desert, Namibia. Sedimentary Geology 123, 255–273.
Eckardt, F.D., Drake, N., Goudie, A.S., White, K., Viles, H., 2001. The role of playas in pedogenic gypsum crust formation in the Central Namib Desert: a theoretical model. Earth Surface Processes and Landforms 26, 1177–1193.
El Tabakh, M., Utha-Aroon, C., Schreiber, B.C., 1999. Sedimentology of the Cretaceous Maha Sarakham evaporites in the Khorat Plateau of northeastern Thailand. Sedimentary Geology 123, 31–62.
Evans, R., Kirkland, D.W., 1988. Evaporitic environments as a source for petroleum. In: Schreiber, B.C. (Ed.), Evaporites and Hydrocarbons. Columbia University Press, New York, pp. 256–299.
Fernandez, O., Olaiz, A., Cascone, L., Hernandez, P., de Peireira, A.F., Tritlla, J., Ingles, M., Aida, B., Pinto, I., Rocca, R., Sanders, C., Herrà, A., Tur, N., 2020. Geophysical evidence for break-up volcanism in the Angola and Gabon passive margins. Marine and Petroleum Geology 116, 104–330.
Fontes, J.-C., Filly, A., Gaudant, J., Duringer, P., 1991. Origine continentale des evaporites Paléogènes de Haute Alsace: arguments paléoécologiques, sédimentologiques et isotopiques. Bulletin de la Société Géologique de France 162, 725–737.
Garrett, D.E., 1970. The chemistry and origin of potash deposits. Third International Symposium on Salt1. Northern Ohio Geological Society, Cleveland, Ohio, pp. 211–222.
Gindre-Chanu, L., Warren, J.K., Puigdefabregas, C., Sharp, I.R., Peacock, D.C.P., Swart, R., Poulsen, R., Ferreira, H., Henrique, L., 2016. Diagenetic evolution of Aptian evaporites in the Namibe Basin (South-West Angola). Sedimentology 62, 204–233.
Gornitz, V.M., Schreiber, B.C., 1981. Displacive halite hoppers from the Dead Sea: some implications for ancient evaporite deposits. Journal of Sedimentary Petrology 51, 787–794.
Grosdidier, E., Braccini, E., Dupont, G., Moron, J.-M., 1996. Biozonation du Cretace inferieur non marin des bassins du Gabon et du Congo: Geologie de l'Afrique et de l'Atlantique Sud. Actes Colloques, Angers, pp. 67–82.
Hardie, L.A., 1984. Evaporites: marine or non-marine ? American Journal of Science 284, 193–240.
Hardie, L.A., 1990. The roles of rifting and hydrothermal $CaCl_2$ brines in the origin of potash evaporites: an hypothesis. American Journal of Science 290, 43–106.
Hardie, L.A., 1996. Secular variation in seawater chemistry: an explanation for the coupled secular variation in the mineralogies of marine limestones and potash evaporites over the past 600 m.y. Geology 24, 279–283.
Hardie, L.A., Lowenstein, T.K., Spencer, R.J., 1985. The problem of distinguishing betweenprimary and secondary features in evaporites. In: Schreiber, B.C., Harner, H.L. (Eds.), Sixth International Symposium on Salt. Salt Institute, Alexandria, Virginia, pp. 11–38.
Hirlemann, G., 1993. Pendagemétrie directe et indirecte - Comparaison et contribution à la résolution de la gîtologie des niveaux sylvinitiques dans la série du bassin côtier congolais. Géologues 100-101, 42–48.
Hirlemann, G., Jaillard, L., 1993. Paléogéographie et diagraphie. Reconstitution de la série salifère de la Loémé, Congo à partir des diagraphies disponibles. Géologues 100-101, 55–58.
Holser, W.T., 1966. Bromide geochemistry of salt rocks. In: Rau, J.L. (Ed.), Second Symposium on Salt 2, pp. 248–275 (Northem Ohio).
Holt, R.M., Powers, D.W., 1990. Geological Mapping of the Air Intake Shaft at the Water Isolation Pilot Plant. Westinghouse Electric Corporation, Carlsbad (495 pp.).
Holt, R.M., Powers, D.W., 2011. Synsedimentary dissolution pipes and the isolation of ancient bacteria and cellulose. Geological Society of America Bulletin 123, 1513–1523.
Hourcq, V., Devigne, J.P., 1950. Notice explicative sur la feuille Port-Gentil ouest, l'A.E.F. Carte géologique de reconnaissance au 1/500 000. Gouvernement Général de l'A.E.F, Paris.
Hovland, M., Rueslåtten, H.G., Johnsen, H.K., Kvamme, B., Kuznetsova, T., 2006. Salt formation associated with sub-surface boiling and supercritical water. Marine and Petroleum Geology 23, 855–869.
Hovorka, S.D., Knauth, L.P., Fischer, R.S., Gao, G., 1993. Marine to nonmarine facies transition in Permian evaporites of the Palo Duro Basin, Texas: geochemical response. Geological Society of America Bulletin 105, 1119–1134.
Hovorka, S.D., Holt, R.M., Powers, D.W., 2007. Depth indicators in Permian Basin evaporites. In: Schreiber, B.C., Babel, M. (Eds.), Evaporites Through Space and Time. Geological Society of London, Special Publication285, pp. 335–364.
Kiro, Y., Goldstein, S.L., Lazar, B., Stein, M., 2015. Environmental implications of salt facies in the Dead Sea. Geological Society of America Bulletin 128, 824–841.
Koeler, G.D., 1997. The geochemistry and petrogenesis of carnallite and its relationship with its diagenesis of the Devonian Prairie Formation(Ph. D. Thesis)University of Saskatchewan, Saskatchewan (220 pp.).
Koeler, G.D., Kyser, T.K., Danyluk, T., 1990. Stable isotope evidence for the petrogenesis of carnallite in the Middle Devonian Prairie Evaporite Formation, Saskatchewan. Summary of investigations 1990, Saskatchewan Geological Survey, Saskatchewan Energy and Mines, Miscellaneous Report 90-4 (218–222 pp.).
Krupp, R.E., 2005. Formation and chemical evolution of magnesium chloride brines by evaporite dissolution processes. Implications for evaporite geochemistry. Geochimica et Cosmochimica Acta 69, 4283–4299.
Lambert, R., 1967. Esquisse géologique du Bassin Potassique Congolais. Annales des Mines 11, 13–26.
Lowenstein, T.K., Hardie, L.A., 1985. Criteria for the recognition of salt-pan evaporites. Sedimentology 32, 627–644.
Lowenstein, T.K., Spencer, R.J., 1990. Syndepositional origin of potash evaporites: petrographic and fluid inclusion evidence. American Journal of Science 290, 1–42.
Lowenstein, T.K., Timofeeff, M.N., Brennan, S.T., Hardie, L.A., Demicco, R.V., 2001. Oscillations in Phanerozoic seawater chemistry: evidence from fluid inclusions. Science 294, 1086–1088.
Lowenstein, T.K., Hardie, L.A., Timofeeff, M.N., Demicco, R.V., 2003. Secular variation in seawater chemistry and the origin of calcium chloride basinal brines. Geology 31, 857–860.
McIntosh, R.A., Wardlaw, N.C., 1968. Barren halite bodies in the sylvinite mining zone of Esterhazy, Saskatchewan. Canadian Journal of Earth Sciences 5, 1221–1238.
Moretto, R., 1988. Observations of the incorporation of trace elements in halite of Oligocene salt beds, Bourg-en-Bresse Basin, France. Geochemica et Cosmochimica Acta 52, 2809–2814.
Moukandi Nkaya, G.D., Niere, R.R., Mabiala, B., Tathy, C., Nkounkou Tomodiatounga, D., Nganga, D., 2014. Hydrogeological information system elaboration of coastal aquifer AQ-2 of Pointe-Noire, in the South-west of Congo-Brazzaville. British Journal of Applied Science and Technology 4, 3342–3359.
Moukolo, N., 1992. Etat des connaissances actuelles sur l'hydrogéologie du Congo Brazzaville. Hydrogéologie 1-2, 47–58.
Moulin, M., Aslanian, D., Unternehr, P., 2010. A new starting point for the South and Equatorial Atlantic Ocean. Earth-Science Reviews 98, 1–37.
Nunn, J.A., Harris, N.B., 2007. Subsurface seepage of seawater across a barrier: a source of water and salt to peripheral salt basins. Geological Society of America Bulletin 119, 1201–1217.
Pedley, A., Neubert, J., Van der Klaw, S., 2016. Potash deposits in Africa. Episodes 39, 447–457.
Poropat, S.F., Colin, J.-P., 2012. Early Cretaceous ostracod biostratigraphy of eastern Brazil and western Africa: an overview. Gondwana Research 22, 772–798.
Powers, D.W., Hassinger, B.W., 1985. Synsedimentary dissolution pits in halite of the Permian Salado Formation, southeastern New Mexico. Journal of Sedimentary Petrology 55, 769–773.
Pueyo, J.J., Chong, G., Ayora, C., 2017. Lithium saltworks of the Salar de Atacama: a model for MgSO4-free ancient potash deposits. Chemical Geology 466, 173–186.
Qiu, J.T., Zhang, C., Xu, Q.-J., Yao, J.L., 2017. Mapping of carnallite along with semi-quantitative estimation of potassium content of drill cores using hyperspectral imagery. Remote sensing Letters 8, 859–868.
Raup, O.B., Hite, R.J., 1978. Bromine Geochemistry of Chloride Rocks of the Middle Pennsylvanian Paradox Formation of the Hermosa Group, Paradox Basin, Utah and Colorado. U.S. Geological Survey Bulletin 2000-M (117 pp.).
Reyre, D., 1984. Petroleum Characteristics and geological evolution of a passive margin. Example of the Lower Congo-Gabon Basin. Bulletin des Centres de Recherches Exploration-Production Elf-Aquitaine 8 (303–302).
Risacher, F., Fritz, B., 2000. Bromine geochemistry of salr de Uyuni and deeper salt crusts, Central Altiplano, Bolivia. Chemical Geology 167, 373–392.
Roberts, S.M., Spencer, R.J., 1995. Palaeotemperatures preserved in fluid inclusions in halite. Geochimica et Cosmochimica Acta 59, 3929–3942.
Rodriguez, C.R., Jackson, C.A.-L., Rotevatn, A., Francies, M., 2017. Dual tectonic-climatic controls on salt giant deposition in the Santos Basin, offshore Brazil. Geosphere 14, 1–28.
Rosell Ortiz, L., Ortí Cabo, F., 1981-1982. The saline (potash) Formation of the Navarra Basin (Upper Eocene, Spain). Petrology. Revista del Instituto de Investigaciones Geológicas Diputación Provincial35. Universidad de Barcelona, pp. 71–121.
Rosell, L., Pueyo, J.-J., 1997. Second marine evaporitic phase in the south pyrenean foredeep: The Priabonian Potash Basin (Late Eocene: Autochtonous-Allochtonous Zone). In: Busson, G., Schreiber, B.C. (Eds.), Sedimentary Deposition in Rift and Foreland Basins in France and Spain. Columbia University Press, New York, pp. 360–387.
Rouchy, J.M., Blanc-Valleron, M.-M., 2006. Les évaporites: matériaux singuliers, milieux extrêmes. Vuibert, Paris (190 pp.).
Schreiber, B.C., 1988. Evaporites and Hydrocarborns. Columbia University Press, New York (475 pp.).
Schreiber, B.C., El Tabakh, M., 2000. Deposition and Early Alteration of Evaporites. Sedimentology 47, 215–238.
Schubel, K.A., Lowenstein, T.K., 1997. Criteria for the recognition of shallow-perennial-saline-lake halite based on recent sediments from the Qaidam Basin, Western China. Journal of Sedimentary Geology 67, 74–87.
Shearman, D.J., 1970. Recent halite rock, Baja California, Mexico. Transactions of the Institution of Mining and Metallurgy 79, 155–162.
Siemann, M.G., 2003. Extensive and rapid changes in seawater chemistry during the Phanerozoic: evidence from Br contents of basal halite. Terra Nova 15, 243–248.
Sirota, I., Arnon, A., Lensky, N.G., 2016. Seasonal variations of halite saturation in the Dead Sea. Water Resources Research 52, 7151–7162.
Sirota, I., Enzel, Y., Lensky, N.G., 2017. Temperature seasonality control on modern halite layers in the Dead Sea: in situ observations. Bulletin of the Geological Society of America 129, 1181–1194.
Sirota, I., Enzel, Y., Lensky, N.G., 2018. Halite focusing and amplification of salt layer thickness: from the Dead Sea to deep hypersaline basins. Geological Society of America Bulletin 2, 851–854.
Sirota, I., Enzel, Y., Mor, Z., Ben Moshe, L., Eyal, H., Lowenstein, T.K., Lensky, N.G., 2020. Sedimentology and stratigraphy of a modern halite sequence formed under Dead Sea level fall. Sedimentology 68, 1069–1090.
Spencer, R.J., Lowenstein, T.K., Casas, E., Pengxi, Z., 1990. Origin of potash salts and brines in the Qaidam Basin, China. In: Eugster, N.P., Spencer, R.J., Ming Chou, I. (Eds.), Fluid-mineral Interactions. The Geochemical Society of London, Special Publication2, pp. 395–408.
SRK Consulting, 2011. NI 43-101 Technical Report Sintoukola Potash Project Republic of Congo. Ercosplan internal report, Erfurt, Germany (158 pp.).
SRK Consulting, 2012. NI 43-101 Technical Report Sintoukola Potash Project Republic of Congo. Ercosplan internal report, Erfurt, Germany (298 pp.).
Szatmari, P., Carvalho, R.S., Simoes, I.A., 1979. A comparison of Evaporite Facies in the Late Palaeozoic Amazon and the Middle Cretaceous South Atlantic Salt Basins. Geology 74, 432–447.

Szatmari, P., Tibana, P., Simões, I.A., Carvalho, R.S., Leite, D.C., 2009. Atlas petrográfico dos evaporites. In: Mohriak, W., Szatmari, P., Anjos, S.M.C. (Eds.), Sal: Geologia e Tectônica: Examplos nas Bacias Brasileiras Beca, São Paulo, pp. 42–63.

Szatmari, P., Moré de Lima, C., Fontaneta, G., de Melo Lima, N., Zambonato, E., Menezes, M. R., Bahniuk, J., Coelho, S.L., Figueiredo, M., Florencio, C.P., Gontijo, R., 2021. Petrography, geochemistry and origin of South Atlantic evaporites: the Brazilian side. Marine and Petroleum Geology 127, 105–143.

Teisserenc, P., Villemin, J., 1990. Sedimentray Basin of Gabon – Geology and oil systems. In: J.D. Edwards, P.A., Santogrossi, M. (Eds.), Divergent/Passive margin Basins. American Association of Petroleum Geologists Memoir48, pp. 117–199.

Timofeeff, M.N., Lowenstein, T.K., da Silva, M.A.M., Harris, N.B., 2006. Secular variation in the major-ion chemistry of seawater: evidence from fluid inclusions in Cretaceous halites. Geochimica et Cosmochimica Acta 70, 1977–1994.

Torsvik, T.H., Rousse, S., Labails, C., Smethurst, M.A., 2009. A new scheme for the opening of the South Atlantic Ocean and the dissection of an Aptian salt basin. Geophysical Journal International 177, 1315–1333.

Urai, J.L., Boland, J.N., 1985. Development of microtextures and the origin of hematite in naturally deformed carnallite. Neues Jahrbuch für Mineralogie Mh. H2 258–272.

Urai, J.L., Schleder, Z., Spiers, C.J., Kukla, P.A., 2008. Flow and transport properties of Salt Rocks. In: Littke, R., Bayer, U., Gajewski, D., Nelskamp, S. (Eds.), Dynamic of Complex Intracontinental Basins: The Central European Basin System. Springer-Verlag, Berlin, pp. 277–290.

Valyashko, M.G., 1956. Geochemistry of Bromine in the processes of salt deposition and the use of the bromine content as a genetic and prospecting criterion. Geochemistry 6, 570–589.

Van Der Klauw, S., Jockel, A., Neubert, J., Rauche, H., 2019. Potash exploration on both side of South Atlantic - Similarities and differences in the deposits and how these influence their appraisal. World of Mining: Surface and Underground 71, 328–343.

Wardlaw, N.C., 1968. Carnallite-Sylvite Relationships in the Middle Devonian Prairie Evaporite Formation, Saskatchewan. Geological Society of America Bulletin 79, 1273–1294.

Wardlaw, N.C., 1972. Unusual marine evaporites with salts of calcium and magnesium chloride in Cretaceous basins of Sergipe, Brazil. Economic Geology 67, 156–168.

Wardlaw, N.C., Nicholls, G.D., 1972. Cretaceous evaporites of Brazil and West Africa and their bering on the theory of continental separation. Proceedings International Geological Congress, 24th Session, Section 6, Montreal, Canada pp. 43–44.

Wardlaw, N.C., Schwerdtner, W.M., 1966. Halite-Anhydrite Seasonal Layers in the Middle Devonian Prairie Evaporite Formation, Saskatchewan, Canada. Geological Society of America Bulletin 77, 331–342.

Warren, J.K., 1986. Shallow-water evaporitic environments and their source rock potential. Journal of Sedimentary Petrology 56 (3), 442–454.

Warren, J.K., 2006. Evaporites: Sediments Resources and Hydrocarbons. Springer-Verlag, Berlin (1036 pp.).

Weiler, Y., Sass, E., Zak, I., 1974. Halite oolites and ripples in the Dead Sea, Israel. Short communication, Sedimentology 21, 623–632.

Zhang, H., Lü, F., Mischke, S., Fan, M., Zhang, F., Liu, C., 2017. Halite fluid inclusions and the late Aptian sea surface temperatures of the Congo Basin, northern South Atlantic Ocean. Cretaceous Research 71, 85–95.

Zhiqiang, X., Parnell, J., 1993. Potash cement in modern and ancient halite beds. Carbonates and Evaporites 8, 149–155.